

Antikaon production in $A + A$ collisions at SIS energies within an off-shell G -matrix approach*

W. Cassing¹, L. Tolós², E. L. Bratkovskaya³, A. Ramos²

¹Institut für Theoretische Physik, Universität Giessen
D-35392 Giessen, Germany

²Departament d'Estructura i Constituents de la Matèria,
Universitat de Barcelona,
Diagonal 647, 08028 Barcelona, Spain

³Institut für Theoretische Physik, Universität Frankfurt/M
D-60054 Frankfurt, Germany

Abstract

The production and propagation of antikaons – described by dynamical spectral functions $A_h(X, \vec{P}, M^2)$ as evaluated from a coupled channel G -matrix approach – is studied for nucleus-nucleus collisions at SIS energies in comparison to the conventional quasi-particle limit and the available experimental data using off-shell transport theory. We find that the K^- spectra for $^{12}\text{C} + ^{12}\text{C}$ and $^{58}\text{Ni} + ^{58}\text{Ni}$ at 1.8 A·GeV remain underestimated in the G -matrix approach as in the on-shell quasi-particle approximation whereas the preliminary spectra for $\text{Au} + \text{Au}$ at 1.5 A·GeV are well described in both limits. This also holds approximately for the K^- rapidity distributions in semi-central collisions of $\text{Ni} + \text{Ni}$ at 1.93 A·GeV. However, in all limits considered there is no convincing description of all spectra simultaneously. Our off-shell transport calculations, furthermore, demonstrate that the strongest in-medium effects should be found for low antikaon momenta in the center-of-mass frame, since the deceleration of the antikaons in the attractive Coulomb and nuclear potentials and the propagation to the on-shell mass induces a net shift and squeezing of the K^- spectra to the low momentum regime.

PACS: 24.10.Cn; 24.10.-i; 25.75.-q; 13.75.Jz

Keywords: Many-body theory; Nuclear-reaction models and methods;
Relativistic heavy-ion collisions; $\bar{K}N$ interaction

*supported by DFG and GSI Darmstadt

1 Introduction

An open problem of today's strong interaction physics is the dynamical generation of hadron masses from the quark and gluon fields, that are the elementary fields of Quantum-Chromo-Dynamics (QCD). Whereas QCD lattice calculations nowadays give quite reliable results for the masses of the 0^- and 1^- meson octet states - except for the light pions - as well for the baryon octet and decuplet states, the masses and properties of these states are not well known at finite quark chemical potential μ_q or finite baryon density ρ_B . This is essentially due to the problem of calculating the fermion determinant at finite μ_q . Though some recent progress has been made for QCD lattice calculations at finite baryon density [1, 2], the properties of hadrons in a baryonic environment cannot be addressed directly so far by such *ab-initio* calculations. One thus presently has to rely on effective hadronic Lagrangians and to compute the hadron properties at finite density ρ_B and/or temperature T by 'dressing' the vacuum states in the medium e.g. within G -matrix theory. An alternative way is to employ effective chiral Lagrangians and to extract the leading order effects for the hadron modifications in the medium.

As demonstrated in the pioneering work of Kaplan and Nelson [3, 4] within a chiral approach kaons and antikaons couple attractively to the scalar nucleon density with a strength proportional to the $KN - \Sigma$ constant,

$$\Sigma_{KN} = \frac{1}{2}(m_u^0 + m_s^0) \langle N|\bar{u}u + \bar{s}s|N \rangle, \quad (1)$$

which may vary from 270–450 MeV (cf. the discussion in Ref. [5]). QCD lattice calculations here provide further information [6]. In Eq. (1) m_u^0 and m_s^0 denote the bare masses for the light u - and strange s -quark while the expression in the brackets is the expectation value of the scalar light and strange quark condensate for the nucleon [7]. Furthermore, a vector coupling to the quark 4-current - for vanishing spatial components - leads to a repulsive potential term for the kaons; this (Weinberg-Tomozawa) term is attractive for the antikaons.

In relativistic mean-field models the dispersion relation for kaons and antikaons in the nuclear medium - for low momenta - can be written as [8, 9, 10]

$$\omega_{K^\pm}(\rho_N, \mathbf{p}) = \pm \frac{3\rho_N}{8f_\pi^2} + \left[\mathbf{p}^2 + m_K^2 \left(1 - \frac{\Sigma_{KN}}{f_\pi^2 m_K^2} \rho_s + \left(\frac{3\rho_N}{8f_\pi^2 m_K} \right)^2 \right) \right]^{1/2}. \quad (2)$$

In Eq. (2) m_K denotes the bare kaon mass, $f_\pi \approx 93$ MeV is the pion decay constant, while ρ_s and ρ_N stand for the scalar and vector nucleon densities, respectively. Note that, when extrapolating Eq. (2) to $3\rho_0$ and above, the antikaon mass becomes very light. Thus antikaon condensates might occur at high baryon density which, furthermore, are of interest in the astrophysical context [11, 12, 13, 14].

Studies on K^\pm production from nucleus-nucleus collisions at SIS energies of 1– 2 A-GeV have shown that in-medium properties of kaons are seen in the collective flow pattern of K^+ mesons, both in-plane and out-of-plane, as well as in the abundance and spectra of antikaons [7, 15, 16, 17, 18, 19]. Thus in-medium modifications of the mesons have

become a topic of substantial interest in the last decade triggered in part by the early suggestion of Brown and Rho [20], that the modifications of hadron masses should scale with the scalar quark condensate $\langle q\bar{q} \rangle$ at finite baryon density.

The actual kaon and antikaon self energies (or potentials) are quite a matter of debate and depend on the many-body resummation scheme adopted. Especially for the antikaons the momentum-dependence of their self energies is widely unknown since most Lagrangian models restrict to s -wave interactions or only include additional p -waves [21, 22, 23]. Here only limited information is available from a dispersion analysis in Ref. [24].

There have been attempts to extract the antikaon-nucleus potential from the analysis of kaonic-atom data and some solutions favor very strongly attractive potentials of the order of -200 MeV at normal nuclear matter density ρ_0 [25, 26]. However, more recent self-consistent calculations based on a chiral Lagrangian [27, 28] or meson-exchange potentials [29] only predict moderate attractive depths of -50 to -80 MeV at density ρ_0 . In addition, studies of kaonic atoms using the chiral $\bar{K}N$ amplitudes of Ref. [30] show that it is indeed possible to find a reasonable reproduction of the data with a relatively shallow antikaon-nucleus potential [31, 32], albeit adding an additional moderate phenomenological part [33]. This has been corroborated by a calculation in Ref. [34], where a good fit to both scattering K^-p data and kaonic-atom data only required to modify slightly the parameters of the chiral meson-baryon interaction model of Ref. [35]. Since it is clear that kaonic atom data do not suitably constrain the antikaon-nucleus potential at normal nuclear matter density, a recent work [36] explored the possibility of distinguishing between deep or shallow potentials [25, 28, 33] by means of nuclear scattering of low energy K^- produced from Φ decay at $\text{Da}\Phi\text{ne}$.

In fact, the antikaon-nucleon amplitude in the isospin channel $I = 0$ is dominated by the $\Lambda(1405)$ resonant structure, which in free space appears only 27 MeV below the $\bar{K}N$ threshold. This resonance is generated dynamically from a coupled channel T -matrix scattering equation using a suitable meson-baryon potential. The coupling between the $\bar{K}N$ and πY ($Y = \Lambda, \Sigma$) channels is essential to get the right dynamical behavior in free space. Correspondingly, the in-medium properties of the $\Lambda(1405)$, such as its pole position and its width, which in turn influence strongly the behavior of the antikaon-nucleus optical potential, are very sensitive to the many-body treatment of the medium effects. Previous works have shown, for instance, that a self-consistent treatment of the \bar{K} self energy has a strong influence on the scattering amplitudes [27, 28, 29, 37] and, consequently, on the in-medium properties of the antikaon. Moreover, the incorporation of the pion with its medium modified properties also proved to be an important aspect [28, 38], although most works until now have ignored it. As pointed out in Ref. [39] also the properties of the $\Sigma^*(1385)$ might be essential for in-medium transitions rates at finite relative momentum since the $\Sigma^*(1385)$ is the strange analogue to the $\Delta(1232)$.

Furthermore, a sizeable progress in the understanding of hadron off-shell propagation in phase-space – even for complex configurations – has been obtained in the last years. In Refs. [40, 41] a semiclassical transport approach has been developed on the basis of the Kadanoff-Baym equations that includes the propagation of hadrons with dynamical spectral functions. This approach has been examined for nucleus-nucleus collisions at GANIL

[40], SIS and AGS energies [41] as well as for equilibration phenomena in related infinite nuclear matter problems [42]. Formally, the input for the off-shell transport approach with respect to the complex hadron self energies and the various channel transition probabilities should be provided by coupled-channel G -matrix calculations. Though being far from complete, the present work makes a major step in this direction by incorporating the off-shell information from $\bar{K}N \leftrightarrow Y\pi$ transitions.

The paper is organized as follows: In Section 2 we will briefly review the generalized transport equations on the basis of the Kadanoff-Baym equations [43] and present the dynamical equations of motion for 'test-particle' propagation in 8-dimensional phase space in comparison to the traditional on-shell equations of motion. The input for this approach relates to self-consistent self energies for the hadrons which here are taken from the coupled-channel G -matrix approach following Ref. [38] (Section 3). The actual description of in-medium kaon and antikaon production in NN and πN collisions - in line with the \bar{K} spectral function from the G -matrix approach - is described in Section 4. The explicit transport calculations for nucleus-nucleus collisions in the SIS energy regime are presented in Section 5 in comparison to the experimental data available. A summary and discussion of open problems concludes this study in Section 6.

2 Description of the off-shell transport approach

Whereas the equilibration of strongly interacting quantum systems has been studied on the basis of the Kadanoff-Baym equations [43] for infinite nuclear matter problems quite some time ago [44] the question how to propagate 'broad resonances' in an inhomogeneous medium out-of-equilibrium (as encountered in relativistic nucleus-nucleus collisions), has been addressed and solved only in the last years [40, 41, 42, 45, 46, 47, 48, 49]. In the latter works a semi-classical off-shell transport approach has been derived from the Wigner transformed Kadanoff-Baym equations in the limit of first order gradients in phase space. The approach by Ivanov et al. in Refs. [46, 47, 48, 49] differs from those in Refs. [40, 41, 42, 45] in the treatment of the 'rearrangement term', which is kept in all orders in Refs. [46, 47, 48, 49], but only employs first order phase-space gradients in Refs. [40, 41, 42, 45] as suggested by Botermans and Malfliet already in 1990 [50]. The latter limit allows to perform a test-particle solution to the problem, which is adequate for present transport approaches, whereas the transport equations from Ivanov et al. [46, 47, 48, 49] might only be solved on a 8-dim. grid in phase space which is very inconvenient for actual applications. A recent overview on the different approaches has been given in Ref. [49].

We here follow the off-shell approach developed in Refs. [40, 41, 42]. For the actual details we refer the reader to the original articles or independently to Ref. [45] for a nonrelativistic formulation. We now concentrate on those results that are important for our present study. First of all, the transport limit provides an algebraic result for the

hadron spectral function

$$A_{XP} = \frac{\Gamma_{XP}}{(P^2 - M_0^2 - \text{Re}\Sigma_{XP}^{\text{ret}})^2 + \Gamma_{XP}^2/4}, \quad (3)$$

which holds for all approaches [40, 41, 42, 45, 46, 47, 48, 49]. In Eq. (3) M_0 denotes the bare mass pole, $\Gamma_{XP} = -2\text{Im}\Sigma_{X,P}^{\text{ret}}$ while $\Sigma_{X,P}^{\text{ret}}$ is the retarded self energy of the hadron which in general depends on space-time X and the four-momentum P in a hadronic environment.

2.1 Testparticle representation

In order to obtain an approximate solution to the transport equation ((16) in Ref. [41]) we use a testparticle ansatz for the Green function $S_{XP}^<$, i.e. for the Wigner transform of

$$i S_{xy}^< := \langle \Phi^\dagger(y) \Phi(x) \rangle, \quad (4)$$

with $X = (x + y)/2$, where $\Phi(x), \Phi^\dagger(y)$ denote the hadron field operators at space-time position x or y . More specifically, we rewrite $iS_{XP}^<$ in terms of the real and positive semidefinite quantity

$$F_{XP} = A_{XP}N_{XP} = iS_{XP}^< \sim \sum_{i=1}^N \delta^{(3)}(\vec{X} - \vec{X}_i(t)) \delta^{(3)}(\vec{P} - \vec{P}_i(t)) \delta(P_0 - \epsilon_i(t)), \quad (5)$$

where the spectral function A_{XP} [Eq. (3)] is separated from the number density function N_{XP} . In the most general case (where the self energies depend on four-momentum P , time t and the spatial coordinates \vec{X}) the equations of motion for the testparticles read [41]

$$\frac{d\vec{X}_i}{dt} = \frac{1}{1 - C_{(i)}} \frac{1}{2\epsilon_i} \left[2\vec{P}_i + \vec{\nabla}_{P_i} \text{Re}\Sigma_{(i)}^{\text{ret}} + \frac{\epsilon_i^2 - \vec{P}_i^2 - M_0^2 - \text{Re}\Sigma_{(i)}^{\text{ret}}}{\Gamma_{(i)}} \vec{\nabla}_{P_i} \Gamma_{(i)} \right], \quad (6)$$

$$\frac{d\vec{P}_i}{dt} = -\frac{1}{1 - C_{(i)}} \frac{1}{2\epsilon_i} \left[\vec{\nabla}_{X_i} \text{Re}\Sigma_{(i)}^{\text{ret}} + \frac{\epsilon_i^2 - \vec{P}_i^2 - M_0^2 - \text{Re}\Sigma_{(i)}^{\text{ret}}}{\Gamma_{(i)}} \vec{\nabla}_{X_i} \Gamma_{(i)} \right], \quad (7)$$

$$\frac{d\epsilon_i}{dt} = \frac{1}{1 - C_{(i)}} \frac{1}{2\epsilon_i} \left[\frac{\partial \text{Re}\Sigma_{(i)}^{\text{ret}}}{\partial t} + \frac{\epsilon_i^2 - \vec{P}_i^2 - M_0^2 - \text{Re}\Sigma_{(i)}^{\text{ret}}}{\Gamma_{(i)}} \frac{\partial \Gamma_{(i)}}{\partial t} \right], \quad (8)$$

where the notation $F_{(i)}$ implies that the function is taken at the coordinates of the testparticle, i.e. $F_{(i)} \equiv F(t, \vec{X}_i(t), \vec{P}_i(t), \epsilon_i(t))$.

In Eqs.(6)-(8) the common multiplication factor $(1 - C_{(i)})^{-1}$ contains the energy derivatives of the retarded self energy

$$C_{(i)} = \frac{1}{2\epsilon_i} \left[\frac{\partial}{\partial \epsilon_i} \text{Re}\Sigma_{(i)}^{\text{ret}} + \frac{\epsilon_i^2 - \vec{P}_i^2 - M_0^2 - \text{Re}\Sigma_{(i)}^{\text{ret}}}{\Gamma_{(i)}} \frac{\partial}{\partial \epsilon_i} \Gamma_{(i)} \right] \quad (9)$$

which yields a shift of the system time t to the 'eigentime' of particle i defined by $\tilde{t}_i = t/(1 - C_{(i)})$. As in Refs. [41, 42] we will assume $C_{(i)} = 0$ furtheron. We mention, that the approximation $C_{(i)} = 0$ is also employed in the more standard transport models that operate with on-shell quasi-particles. In the limiting case of particles with vanishing gradients of the width Γ_{XP} the equations of motion (6) - (8) reduce to the well-known transport equations of the quasi-particle picture.

Furthermore, following Ref. [40] we take $M^2 = P^2 - Re\Sigma^{ret}$ as an independent variable instead of P_0 , which then fixes the energy (for given \vec{P} and M^2) to

$$P_0^2 = \vec{P}^2 + M^2 + Re\Sigma_{X\vec{P}M^2}^{ret}. \quad (10)$$

Eq. (8) then leads to

$$\frac{dM_i^2}{dt} = \frac{M_i^2 - M_0^2}{\Gamma_{(i)}} \frac{d\Gamma_{(i)}}{dt} \quad (11)$$

for the time evolution of the test-particle i in the invariant mass squared as derived in Ref. [41]. It is worth noting that Eq. (11) (for $\Gamma_{(i)} \neq 0$) is equivalent to

$$\frac{d}{dt} \left(\frac{M_i^2 - M_0^2}{\Gamma_{(i)}} \right) = 0, \quad (12)$$

which states that the ratio of $\Delta M_i^2 = M_i^2 - M_0^2$ to the actual width $\Gamma_{(i)}$ is a constant in time.

2.2 Collision terms

The collision term of the Kadanoff-Baym equation in first order gradient expansion reads as [41]

$$\begin{aligned} I_{coll}(X, \vec{P}, M^2) &= Tr_2 Tr_3 Tr_4 A(X, \vec{P}, M^2) A(X, \vec{P}_2, M_2^2) A(X, \vec{P}_3, M_3^2) A(X, \vec{P}_4, M_4^2) \\ &|G((\vec{P}, M^2) + (\vec{P}_2, M_2^2) \rightarrow (\vec{P}_3, M_3^2) + (\vec{P}_4, M_4^2))|_{\mathcal{A}, \mathcal{S}}^2 \delta^{(4)}(P + P_2 - P_3 - P_4) \\ &[N_{X\vec{P}_3M_3^2} N_{X\vec{P}_4M_4^2} \bar{f}_{X\vec{P}M^2} \bar{f}_{X\vec{P}_2M_2^2} - N_{X\vec{P}M^2} N_{X\vec{P}_2M_2^2} \bar{f}_{X\vec{P}_3M_3^2} \bar{f}_{X\vec{P}_4M_4^2}] \end{aligned} \quad (13)$$

with

$$\bar{f}_{X\vec{P}M^2} = 1 + \eta N_{X\vec{P}M^2} \quad (14)$$

and $\eta = \pm 1$ for bosons/fermions, respectively. The indices \mathcal{A}, \mathcal{S} stand for the antisymmetric/symmetric matrix element of the in-medium scattering amplitude G in case of fermions/bosons. In Eq. (13) the trace over particles 2,3,4 reads explicitly for fermions

$$Tr_2 = \sum_{\sigma_2, \tau_2} \frac{1}{(2\pi)^4} \int d^3P_2 \frac{dM_2^2}{2\sqrt{\vec{P}_2^2 + M_2^2}}, \quad (15)$$

where σ_2, τ_2 denote the spin and isospin of particle 2. In case of bosons we have

$$Tr_2 = \sum_{\sigma_2, \tau_2} \frac{1}{(2\pi)^4} \int d^3 P_2 \frac{dP_{0,2}^2}{2}, \quad (16)$$

since the spectral function A_B is normalized as

$$\int \frac{dP_0^2}{4\pi} A_B(X, P) = 1 \quad (17)$$

whereas for fermions we get

$$\int \frac{dP_0}{2\pi} A_F(X, P) = 1. \quad (18)$$

Here the spectral function A_F in case of fermions in Eq. (13) is obtained by considering only particles of positive energy and assuming the spectral function to be identical for spin 'up' and 'down' states.

We note that the extension of Eq. (13) to inelastic scattering processes (e.g. $\bar{K}N \rightarrow Y\pi$) or ($\pi Y \rightarrow \bar{K}N$ etc.) is straightforward when exchanging the elastic transition amplitude G by the corresponding inelastic one and taking care of Pauli-blocking or Bose-enhancement for the particles in the final state. For bosons we will neglect a Bose-enhancement factor throughout this work since their actual phase-space density is small for the systems of interest.

Thus the transport approach and the particle spectral functions are fully determined once the in-medium transition amplitudes G are known *in their full off-shell dependence*. For the transitions $NN \rightarrow NN$ and $N\Delta \leftrightarrow NN$ we employ the same approximations as in Ref. [41] whereas for the strangeness sector $\bar{K}N \leftrightarrow \bar{K}N$ and $\bar{K}N \leftrightarrow \pi Y$ we will use the off-shell transition rates as determined from the coupled channel G -matrix approach to be described below.

3 The coupled-channel G -matrix approach

In Ref. [29], the effective $\bar{K}N$ interaction in the nuclear medium (G -matrix) at temperature $T = 0$ was derived from a meson-baryon bare interaction built in the meson exchange framework [51]. As the bare interaction permits transitions from the $\bar{K}N$ channel to the $\pi\Sigma$ and $\pi\Lambda$ ones, all having strangeness $S = -1$, one is confronted with a coupled-channel problem. Working in an isospin coupled basis, the $\bar{K}N$ channel can have isospin $I = 0$ or $I = 1$, so the resultant G -matrices are classified according to the value of isospin. For $I = 0$, $\bar{K}N$ and $\pi\Sigma$ are the only channels available, while for $I = 1$ the $\pi\Lambda$ channel is also allowed. In a schematic notation, each G -matrix fulfills the coupled channel equation:

$$\begin{aligned} \langle M_1 B_1 | G(\Omega) | M_2 B_2 \rangle &= \langle M_1 B_1 | V(\sqrt{s}) | M_2 B_2 \rangle \\ &+ \sum_{M_3 B_3} \langle M_1 B_1 | V(\sqrt{s}) | M_3 B_3 \rangle \frac{Q_{M_3 B_3}}{\Omega - E_{M_3} - E_{B_3} + i\eta} \langle M_3 B_3 | G(\Omega) | M_2 B_2 \rangle, \quad (19) \end{aligned}$$

where Ω is the 'starting energy', given in the lab. frame, and \sqrt{s} is the invariant center-of-mass energy. In Eq. (19), M_i and B_i represent, respectively, the possible mesons (\bar{K} , π) and baryons (N , Λ , Σ), and their corresponding quantum numbers, such as coupled spin and isospin, and linear momentum. The function $Q_{M_3 B_3}$ stands for the Pauli operator preventing the nucleons in the intermediate states from occupying already filled states.

The prescription for the single-particle energies of all the mesons and baryons participating in the reaction and in the intermediate states is written - in nonrelativistic approximation but keeping relativistic kinematics - as

$$E_{M_i(B_i)}(p) = \sqrt{p^2 + m_{M_i(B_i)}^2} + U_{M_i(B_i)}(p, E_{M_i(B_i)}^{qp}(p)) , \quad (20)$$

where $U_{M_i(B_i)}$ is the single-particle potential of each meson (baryon) calculated at the real quasi-particle energy $E_{M_i(B_i)}^{qp}$. For baryons, this quasi-particle energy is given by

$$E_{B_i}^{qp}(p) = \sqrt{p^2 + m_{B_i}^2} + U_{B_i}(p) , \quad (21)$$

while, for mesons, it is obtained by solving the implicit equation

$$(E_{M_i}^{qp}(p))^2 = p^2 + m_{M_i}^2 + \text{Re} \Sigma_{M_i}^{ret}(p, E_{M_i}^{qp}(p)) , \quad (22)$$

where $\Sigma_{M_i}^{ret}$ is the retarded meson self energy.

The \bar{K} single-particle potential in the Brueckner-Hartree-Fock approach (at temperature $T = 0$) is given by

$$U_{\bar{K}}(p_{\bar{K}}, E_{\bar{K}}^{qp}) = \sum_{N \leq F} \langle \bar{K}N | G_{\bar{K}N \rightarrow \bar{K}N}(\Omega = E_N^{qp} + E_{\bar{K}}^{qp}) | \bar{K}N \rangle , \quad (23)$$

where the summation over nucleon states is limited to the occupied nucleon Fermi sphere. The \bar{K} self energy is obtained from the optical potential (neglecting energy derivatives) through the relation

$$\Sigma_{\bar{K}}^{ret}(p_{\bar{K}}, \omega) = 2 \sqrt{p_{\bar{K}}^2 + m_{\bar{K}}^2} U_{\bar{K}}(p_{\bar{K}}, \omega) , \quad (24)$$

with $\omega = E_{\bar{K}}^{qp}(p_{\bar{K}})$. As it can be easily seen from Eq. (23), since the $\bar{K}N$ effective interaction (G -matrix) depends on the \bar{K} single-particle energy, which in turn depends on the \bar{K} potential through Eqs. (22),(24), one needs to solve a self-consistent problem.

After self-consistency is reached, the complete energy-and-momentum dependent self energy of the \bar{K} can be obtained from Eq. (24), which allows one to derive the \bar{K} propagator

$$D_{\bar{K}}(p_{\bar{K}}, \omega) = \frac{1}{\omega^2 - p_{\bar{K}}^2 - m_{\bar{K}}^2 - \Sigma_{\bar{K}}^{ret}(p_{\bar{K}}, \omega)} , \quad (25)$$

and the corresponding spectral density, defined as

$$S_{\bar{K}}(p_{\bar{K}}, \omega) = -\frac{1}{\pi} \text{Im} D_{\bar{K}}(p_{\bar{K}}, \omega) . \quad (26)$$

We note that our self-consistent procedure amounts to replace the complex energy dependent self energy, $\Sigma_{\bar{K}}^{ret}(p_{\bar{K}}, \omega)$, in the \bar{K} propagator by that evaluated at the quasi-particle energy, $\Sigma_{\bar{K}}^{ret}(p_{\bar{K}}, \omega = E_{\bar{K}}^{qp}(p_{\bar{K}}))$. We denote this procedure as the *quasi-particle self-consistent approach*, which retains the position and the width of the peak of the \bar{K} spectral function at each iteration. This simplification relative to using the complete energy dependence, as done in Refs. [27, 28], allows one to perform analytically the energy integral of the intermediate loops, thus reducing the four-dimensional integral equation to a three-dimensional one.

An important modification for the antikaon properties comes from considering the pion self energy, $\Sigma_{\pi}^{ret}(p_{\pi}, \omega)$, in the intermediate $\pi\Sigma$, $\pi\Lambda$ states present in the construction of the $\bar{K}N$ effective interaction. Since the dressing of the pions has a strong influence on the antikaon in-medium properties (cf. Refs. [28, 38] and also Sections 3.2 and 5 of the present work), it is of relevance to be more specific on the actual realization. The pion self energy of the present work is built up from ph , Δh and $2p2h$ excitations and contains the effect of nucleon-nucleon short-range correlations via a phenomenological model developed in Refs. [52, 53], which gives rise to a smooth momentum-dependent Landau-Migdal parameter g' of the order of 0.6. This is very similar to the value obtained from microscopic calculations based on the nucleon-nucleon G-matrix [54, 55, 56] including the crossed-channel contributions, similarly as the induced interaction of Babu and Brown [57]. Moreover, the phenomenological pion self energy used here has been tested in various reactions involving the interaction of virtual or real pions with nuclei in Refs. [58, 59, 60, 61]. Certainly, this pion self energy is extrapolated to higher densities in the present work and it might not be justified to use the same value for g' . However, the microscopic study of Ref. [54], performed in the context of the problem of pion condensation at high baryon density, only showed a weak dependence of the nucleon-nucleon residual interaction with density. Nevertheless, we regard the issue of pion dressing at higher baryon densities still to be open and will present our G-matrix results in two limits, i.e. with and without pion dressing.

In order to address energetic nucleus-nucleus collisions, the coupled G -matrix equations in principle have to be extended to non-equilibrium phase-space configurations. This is quite a formidable task such that we restrict to finite temperature calculations since the antikaon dynamics of interest proceeds in the environment of a hot hadronic fireball.

The introduction of temperature in the G -matrix equations affects the Pauli blocking of the intermediate nucleon states as well as the dressing of mesons and baryons. The G -matrix equation at finite T reads formally as in Eq. (19), but replacing (cf. Ref. [38])

$$\begin{aligned} Q_{MB} &\rightarrow Q_{MB}(T) \\ G(\Omega) &\rightarrow G(\Omega, T) \\ E_M, E_B &\rightarrow E_M(T), E_B(T). \end{aligned}$$

The function $Q_{MB}(T)$ is unity for meson-hyperon states while, for $\bar{K}N$ states, it follows

$Q_{MB}(T) = 1 - n(p_N, T, \mu)$ with the nucleon occupation number given by

$$n(p_N, T, \mu) = \left[1 + \exp \left(\frac{E_N(p_N, T) - \mu}{T} \right) \right]^{-1}. \quad (27)$$

The chemical potential μ in Eq. (27) is obtained by imposing the normalization condition for the nucleon density

$$\rho = \frac{g}{(2\pi)^3} \int d^3 p_N n(p_N, T, \mu), \quad (28)$$

where $g = 4$ is the degeneracy factor for symmetric nuclear matter.

A finite temperature also affects the properties of the particles involved in the process. The \bar{K} optical potential at a given temperature T is calculated according to

$$U_{\bar{K}}(p_{\bar{K}}, E_{\bar{K}}^{qp}, T) = \int d^3 p_N n(p_N, T) \langle \bar{K}N | G_{\bar{K}N \rightarrow \bar{K}N}(\Omega = E_N^{qp} + E_{\bar{K}}^{qp}, T) | \bar{K}N \rangle, \quad (29)$$

which again is a self-consistent problem for $U_{\bar{K}}$. More explicitly, using the partial wave components of the G -matrix, we obtain

$$U_{\bar{K}}(p_{\bar{K}}, E_{\bar{K}}^{qp}, T) = \frac{1}{2} \sum_{L,J,I} (2J+1)(2I+1) \int n(p_N, T) p_N^2 dp_N \times \langle (\bar{K}N); \bar{p} | G^{LJI}(\bar{P}, E_{\bar{K}}^{qp}(p_{\bar{K}}) + E_N^{qp}(p_N), T) | (\bar{K}N); \bar{k} \rangle, \quad (30)$$

where \bar{p} and \bar{P} are the relative and center-of-mass momentum, respectively, averaged over the angle between the external \bar{K} momentum in the lab system, $p_{\bar{K}}$, and the internal momentum of the nucleon, p_N . In the actual calculations, we include partial waves up to $L = 4$. In extension of the work in Ref. [38], we here additionally include the $\Sigma^*(1385)$ resonance dynamics in a similar way as in Ref. [23]. We note that the role of this sub-threshold $\Sigma^*(1385)$ resonance is negligible for $\bar{K}N$ free scattering observables but, as suggested in Ref. [39], it can become relevant in the medium since, due to the attraction felt by the antikaons, one is effectively exploring lower values of \sqrt{s} .

3.1 Antikaon quasi-particle properties

With respect to nucleus-nucleus collisions at SIS energies (1–2 A·GeV), we have performed the G -matrix calculations at a fixed temperature $T = 70$ MeV which corresponds to an average temperature of the 'fireballs' produced in these collisions. Moreover, we note that variations in the temperature from 50 - 100 MeV do not sensibly affect the quasi-particle properties in the medium [38].

Whereas in Ref. [38] the antikaon potentials have been shown at the quasi-particle energy (as a function of momentum and nuclear density), we display in Fig. 1 the real part of the antikaon potential $\text{Re } U_{\bar{K}}$ as a function of

$$\sqrt{s} = \sqrt{\omega^2 - p_{\bar{K}}^2}, \quad (31)$$

where ω denotes the antikaon energy and $p_{\bar{K}}$ its momentum relative to the nuclear matter rest frame, for different densities and momenta $p_{\bar{K}} = 0, 150, 300,$ and 500 MeV/c, respectively. The arrows in Fig. 1 show the pole mass of the antikaon in free space for orientation. It is seen from Fig. 1 that the real part of the potential is attractive throughout and approximately linear in the nuclear density from $0.5 \rho_0$ to $2 \rho_0$. Furthermore, the potential is slightly more attractive for smaller off-shell masses than for masses above the free invariant mass. With increasing momentum $p_{\bar{K}}$ the potential becomes shallower and the dip at an invariant mass of ~ 320 MeV vanishes. We note, that the results presented in Fig. 1 stem from a G -matrix calculation including the pion dressing. When excluding pion self energies the antikaon potential becomes even more attractive especially for low invariant masses.

The imaginary part of the antikaon potential $\text{Im } U_{\bar{K}}$ is shown in Fig. 2 also as a function of \sqrt{s} for different densities and momenta $p_{\bar{K}} = 0, 150, 300,$ and 500 MeV/c, respectively. The imaginary part is also roughly proportional to the nuclear density and larger for smaller invariant masses than for masses higher than the free antikaon mass (arrows). The structure observed around $\sqrt{s} \sim 300$ MeV at low momentum is due to resonant p -wave coupling to ΣN^{-1} states as will be discussed below. In general, the imaginary part shows only a weak dependence on the momentum $p_{\bar{K}}$.

The resulting spectral function $S_{\bar{K}}(p_{\bar{K}}, \omega)$ is shown in Fig. 3 as

$$A(p_{\bar{K}}, \sqrt{s}) = 2 \sqrt{p_{\bar{K}}^2 + m_{\bar{K}}^2} S_{\bar{K}}(p_{\bar{K}}, \omega), \quad (32)$$

where \sqrt{s} can be identified with the invariant mass M , for different densities and momenta $p_{\bar{K}} = 0, 150, 300,$ and 500 MeV/c, respectively. In line with Figs. 1 and 2 the maximum of the spectral function shifts to lower invariant masses with increasing density and becomes substantially broader. The relative change with momentum $p_{\bar{K}}$ is only moderate as seen from Fig. 3.

As pointed out in Section 2, the information presented in Figs. 1 and 2 – on a much finer grid in momentum and density – is used for the off-shell propagation of antikaons in the nuclear medium according to the Eqs. (6), (7), (8) in the transport approach. On the other hand, the spectral functions from Fig. 3 – also on a much finer grid in momentum and density – enter the collision terms of Eq. (13) for the production of antikaons in nucleon-baryon, meson-baryon or pion-hyperon interactions.

3.2 In-medium transition rates

Apart from the spectral functions A_{XP} the collision terms in Eq. (13) depend on the local phase-space densities $N_{X\vec{P}M^2}$, that are calculated dynamically for all hadrons, and the transition matrix-elements squared $|G((\vec{P}, M^2) + (\vec{P}_2, M_2^2) \rightarrow (\vec{P}_3, M_3^2) + (\vec{P}_4, M_4^2))|_{\mathcal{A}, \mathcal{S}}^2$. Here the latter have to be known not only for on-shell but also for off-shell particles.

For binary reactions involving antikaons like $\bar{K}N \rightarrow \bar{K}N$ or $\pi\Lambda \leftrightarrow \bar{K}N$ these matrix elements are determined by the G -matrix equation (19) such that no new parameters

or unknown cross sections enter the transport calculations. Actual cross sections are determined as a function of the invariant energy squared s as

$$\sigma_{1+2\rightarrow 3+4}(s) = (2\pi)^5 \frac{E_1 E_2 E_3 E_4 p'}{s p} \int d\cos(\theta) \frac{1}{(2s_1 + 1)(2s_2 + 1)} \sum_i \sum_\alpha G^\dagger G, \quad (33)$$

where p and p' denote the center-of-mass momentum of the particles in the initial and final state, respectively. The sums over i and α indicate the summation over initial and final spins, while s_1, s_2 are the spins of the particles in the entrance channel. Apart from the kinematical factors, the transition rates are determined by the angle integrated average transition probabilities

$$P_{1+2\rightarrow 3+4}(s) = \int d\cos(\theta) \frac{1}{(2s_1 + 1)(2s_2 + 1)} \sum_i \sum_\alpha G^\dagger G \quad (34)$$

which are uniquely determined by the G -matrix elements evaluated for finite density ρ , temperature T and relative momentum $p_{\bar{K}}$ with respect to the nuclear matter rest frame.

Before coming to the actual in-medium problem we show in Fig. 4 a comparison of our calculations for the strangeness exchange cross sections $K^-p \rightarrow \Sigma^0\pi^0$, $K^-p \rightarrow \Sigma^+\pi^-$, $K^-p \rightarrow \Lambda\pi^0$, and $K^-p \rightarrow \Sigma^-\pi^+$ in 'free space' with the corresponding experimental data from [62] as a function of the antikaon momentum $p_{\bar{K}}$ in the laboratory. As seen from Fig. 4 we miss the small resonance for $p_{\bar{K}} \approx 0.4$ GeV/c in the $K^-p \rightarrow \Sigma^0\pi^0$ channel¹ and slightly overestimate the $K^-p \rightarrow \Lambda\pi^0$ channel. Otherwise, the comparison shows that our transition probabilities are sufficiently realistic for the vacuum cross sections. It should be pointed out, that the $\Lambda(1405)$ is generated dynamically in our approach whereas in Refs. [63, 64] it is treated as an elementary field.

We now turn to the transition probabilities of Eq. (34) at finite density ρ , finite temperature T and finite antikaon momentum $p_{\bar{K}}$ in the nuclear matter rest frame. They are displayed in Figs. 5, 6, 7 and 8 for the reactions $K^-p \rightarrow K^-p$, $K^-p \rightarrow \Sigma^0\pi^0$, $K^-p \rightarrow \Lambda\pi^0$ and $\Lambda\pi^0 \rightarrow \Lambda\pi^0$, respectively. The isometric plots show the probabilities of Eq. (34) as a function of density ρ (in units of ρ_0) and \sqrt{s} for a momentum $p_{\bar{K}} = 0$ at $T = 70$ MeV. The results on the l.h.s. correspond to a G -matrix calculation without pion dressing whereas those on the r.h.s. include pion dressing as described in Section 3. We note that the general shape of these transition probabilities does not change very much at finite momentum $p_{\bar{K}}$ such that we discard an explicit representation over this variable.

In order to pick up the physics from Figs. 5-8 we recall that the K^-p threshold in free space corresponds to $\sqrt{s} \approx 1.432$ GeV, whereas the thresholds for $\pi^0\Lambda$ and $\pi^0\Sigma$ are at 1.25 GeV and 1.332 GeV, respectively. In free space ($\rho = 0$) the coupling to the $\Lambda(1405)$ resonance provides the dominant matrix elements below (and close to) the $\bar{K}N$ threshold in all channel amplitudes that contain the $I = 0$ component (Figs. 5 and 6). Note that, in the case of off-shell antikaon dynamics in the nuclear medium, also lower invariant \sqrt{s} become accessible such that a resonant amplitude slightly below the free threshold will give large in-medium transition rates. The same considerations apply to the p -wave Σ^*

¹The $\Lambda(1520)$ is not included in our calculations.

resonance located at 1.385 GeV. Its influence is seen more clearly in the $I = 1$ channel $\Lambda\pi^0 \rightarrow \Lambda\pi^0$ (Fig. 8). The reason is that, since the p -wave amplitude is proportional to the product of center-of-mass momenta in the incoming and outgoing channels, pp' , it gets enhanced for invariant energies above and away of the corresponding thresholds. This also explains the enhanced contribution of this resonance in the channel $K^-p \rightarrow \Lambda\pi^0$ (Fig. 7) as density grows due to the fact that the K^-p threshold, which lies above the $\Sigma^*(1385)$ in free space, also moves to lower energies in the medium. This is especially visible on the l.h.s of Fig. 7 when pion dressing is ignored. In fact, the width of the $\Sigma^*(1385)$ resonance already increases in the medium when only the dressing of the antikaons is incorporated due to the opening of new decay channels, such as $\Sigma^*N \rightarrow \Lambda N, \Sigma N, \pi\Lambda N, \pi\Sigma N$. However, the additional dressing of the pions in the $\pi\Lambda, \pi\Sigma$ G-matrix intermediate states, to which the Σ^* couples very strongly, enhances tremendously its decay width into the above mentioned nucleon-induced channels, hence producing a very 'smeared out' contribution, as observed on the r.h.s. of Fig. 7.

We also note that in the region of the $\pi\Sigma$ threshold the squared matrix amplitudes that contain $I = 0$ components (see Figs. 5 and 6) present a double peak structure at low densities when pion dressing is included. This was already pointed out in Ref. [38], where it was shown that the in-medium $I = 0$ s -wave resonance moves down below the $\pi\Sigma$ threshold at normal nuclear matter density ρ_0 . Hence, as density increases and, for some range of densities, this resonance shows up as two distinct bumps.

In any case, it is clear that, whatever resonant structures are present at low densities, they melt away already at a modest density of $\sim 0.5\rho_0$ for all calculations that include pion dressing (r.h.s.).

Finally, one observes very modest structures, especially visible in the channels that contain $I = 1$ contributions at low energies (see Figs. 7 and 8), which explain the behaviour found in the antikaon potential (cf. Figs. 1 and 2) as well as the bump of the antikaon spectral function (cf. Fig. 3) around $\sqrt{s} \approx 300$ MeV, i.e. roughly 200 MeV below the free \bar{K} mass. These structures correspond to the coupling of the \bar{K} meson to Σ -nucleon hole configurations.

4 Antikaon production from NN and πN collisions

Whereas the G -matrix approach described in the previous subsection uniquely determines the off-shell transitions $\bar{K}N \rightarrow \bar{K}N$ and $\bar{K}N \leftrightarrow \pi Y$, i.e. the dynamics of hadrons with s -quarks in the medium, the production cross sections of kaons and antikaons from NN or πN collisions are not specified accordingly. As already shown in Ref. [65] the latter channels are subdominant relative to the leading s -quark exchange reactions $\pi Y \rightarrow \bar{K}N$. This dominance of the πY reaction channel in nucleus-nucleus collisions at SIS energies is related to the fact that kaon cross sections and (due to strangeness conservation) the hyperon cross sections are about 2 orders of magnitude higher than the antikaon cross sections [65, 66]. Consequently $s\bar{s}$ -quarks are essentially created with KY final channels from $NN, \Delta N$ and πN reactions and a large fraction of antikaons stems from the strange

flavor exchange channels $\pi Y \rightarrow \bar{K}N$. We mention that with increasing bombarding energy also the channel $\pi\pi \rightarrow K\bar{K}$ may contribute significantly for heavy systems [67, 68].

For the determination of the in-medium $NN \rightarrow NNK\bar{K}$ and $\pi N \rightarrow NK\bar{K}$ cross section we here proceed as follows: from experimental data on the 'free' production cross sections we extract an average matrix element squared $|\mathcal{M}|^2$ by dividing out the phase space for on-shell particles in the final state and the flux factor (cf. Ref. [69]). Using the same matrix element, the off-shell cross sections then are obtained by employing the dynamical spectral functions for the hadrons and correcting for the modified final state phase-space for off-shell hadrons. The actual implementation is done as follows: In case of meson production by off-shell baryon-baryon or meson-baryon collisions we either have 2 (e.g. $\pi N \rightarrow K^+\Lambda/\Sigma$), 3 (e.g. $NN \rightarrow K^+\Lambda N$ or $K^+\Sigma N$) or 4 particles (e.g. $NN \rightarrow NNK^+K^-$) in the final channel. Since the final mesons may be off-shell as well, one has to specify the corresponding mass-differential cross sections that depend on the entrance channel and especially on the available energy \sqrt{s} in the entrance channel.

We start with the explicit parametrizations for meson (m) production cross sections given in Ref. [7] for on-shell mesons as a function of the invariant energy \sqrt{s} in case of nucleon-nucleon or pion-nucleon collisions, i.e. $\sigma_{NN \rightarrow mNN}(\sqrt{s})$ or $\sigma_{\pi N \rightarrow mN}(\sqrt{s})$, respectively, that are sufficiently well controlled by experimental data in 'free' space. To this aim we show in Fig. 9 the respective data for $pp \rightarrow K^0\bar{K}^0pp$, $pp \rightarrow K^+K^-pp$ from Refs. [62, 70, 71] and $\pi^-p \rightarrow K^-K^0p$ from Ref. [62] in comparison to our parametrizations. The reader should not worry about the fact that the phase-space oriented parametrization for the pp reactions does not match the 2 lowest points close to threshold since the latter are enhanced by the strong final state interaction in the pp and $\bar{K}p$ final channel in free space. On the other hand, such final state interactions are essentially 'screened' in the nuclear medium (especially at high density) such that the phase-space oriented approximations should hold sufficiently well.

Keeping this concept in mind, the in-medium mass differential cross sections – far above the corresponding thresholds – are approximated by

$$\frac{d\sigma_{NN \rightarrow mNN}(\sqrt{s})}{dM^2} = \sigma_{NN \rightarrow mNN}(\sqrt{s} - \sqrt{s_0^*}) A_m(M^2, p, \rho), \quad (35)$$

where $A_m(M^2, p, \rho)$ denotes the meson spectral function for given invariant mass M^2 , relative momentum p and nuclear density ρ as determined from G -matrix theory in Section 3. In Eq. (35) the threshold energy $\sqrt{s_0^*} = M_0 + M_1^* + M_2^*$ depends on the masses of the hadrons in the final channel, i.e. M_0, M_1^* and M_2^* . Actual events then are selected by Monte-Carlo according to Eq. (35). Close to threshold $\sqrt{s_0^*}$, i.e. for $\sqrt{s} - M_0 - M_1^* - M_2^* \leq 2\Gamma_{tot}$, where M_1^*, M_2^* denote the final off-shell masses of two nucleons, M_0 the meson pole mass and Γ_{tot} its total width, the differential production cross section is approximated by a constant matrix element squared $|\mathcal{M}_m|^2$ times the available phase-space,

$$\frac{d\sigma_{NN \rightarrow mNN}(\sqrt{s})}{dM^2} = |\mathcal{M}_m|^2 A_m(M^2, p, \rho) R_3(s, M^2, M_1^{2*}, M_2^{2*}), \quad (36)$$

where the matrix element $|\mathcal{M}_m|$ is fitted to the on-shell cross section typically from 50 to

500 MeV above threshold. In Eq. (36) the function R_3 denotes the 3-body phase-space integral [72] in case of a mNN final state.

In case of 4 particles in the final state, i.e. in the channel $NN \rightarrow K\bar{K}N_1^*N_2^*$, where the N^* 's denote off-shell nucleons, the differential cross section is approximated by

$$E_1 E_2 E_3 E_4 \frac{d^{12} \sigma_{BB \rightarrow NNM_1 M_2}(\sqrt{s})}{d^3 p_1 d^3 p_2 d^3 p_3 d^3 p_4} = \quad (37)$$

$$\sigma_{BB \rightarrow NNM_1 M_2}(\sqrt{s}) \frac{1}{16 R_4(\sqrt{s})} \delta^4(P_1 + P_2 - p_1 - p_2 - p_3 - p_4),$$

where R_4 denotes the 4-body phase-space integral [72]. Similar strategies have been exploited in case of subthreshold $\bar{K}K$ or even $p\bar{p}$ production in proton-nucleus and nucleus-nucleus collisions in Refs. [41, 65, 73, 74].

The resulting cross sections for K^- production from NN and π^-p collisions using on-shell nucleons and kaons in the final state, however, employing the antikaon spectral functions from the G -matrix approach in Section 3, are displayed in Fig. 10 as a function of \sqrt{s} for different nuclear densities ranging from $0.25 \rho_0$ to $2.25 \rho_0$ in comparison to the cross section in free space (solid lines). With increasing nuclear density the subthreshold production of mesons becomes enhanced considerably relative to the respective vacuum cross section due to a shift of the antikaon pole mass and a broadening of its spectral function (cf. Fig. 3), but the absolute magnitude stays small below threshold even for $\rho \approx 2\rho_0$. We recall again that the πN and NN production channels for $K\bar{K}$ pairs are not the leading channels at SIS energies and minor uncertainties in the off-shell treatment of the production cross sections are unlikely to show up in the final K^- abundancies and spectra [65, 66].

We use isospin symmetry to relate the cross sections for π^-p or pp induced reactions to πN and NN collisions. Furthermore, due to a lack of any experimental information, the $\pi\Delta$ production channel is assumed to be same as the πN channel at the same invariant energy \sqrt{s} . The $N\Delta$ and $\Delta\Delta$ production channels again are taken the same as the NN channel for fixed invariant energy. Apart from interactions between baryons and pions with baryons also meson-meson collisions become important with increasing bombarding energy [67, 68]. We include the $\pi\pi \leftrightarrow K\bar{K}$ channel using the cross section from Ref. [7] and in addition to Ref. [65] also the channel $\pi + K \leftrightarrow K^*$ employing a Breit-Wigner resonance cross section with K^* resonance properties from Ref. [75]. Moreover, the decay $\phi \rightarrow K\bar{K}$ is included in the transport calculation which, however, is found to be subdominant.

Now all matrix elements, self energies and/or cross sections for antikaon production and propagation are specified such that we can continue with the actual transport calculations. We recall, that in case of kaons or antikaons at SIS energies (or charmonia at SPS energies) we treat the latter hadrons perturbatively as in Ref. [65, 76, 77], i.e. each testparticle achieves a weight W_i defined by the ratio of the individual production cross section to the total πB or BB cross section at the same invariant energy. Their propagation and interactions are evaluated as for baryons and pions, however, the baryons (pions) are not changed in their final state when interacting with a 'perturbative' particle.

In case of strange flavor exchange reactions the individual weight of a \bar{K} is given to the hyperon Y and viceversa. In this way exact strangeness conservation can be achieved during the transport calculation while obtaining reasonable statistics also for antikaons at 'subthreshold' energies. We mention again that the actual (space-time dependent) antikaon width is determined by the G -matrix approach described in Section 3.

5 Nucleus-nucleus collisions

We carry out the concrete applications for nuclear reactions at SIS energies (1.5 - 2 A GeV) that have been analysed within conventional transport models to a large extent (cf. Refs. [7, 16] and Refs. therein). However, before coming to the actual results we like to address the off-shell propagation of antikaons and the evolution of the K^- spectral density in time and invariant mass for central nucleus-nucleus collisions. To this aim we show in Fig. 11 the time evolution of the quantity

$$F(M, t) = \int d^3r \int d^3p A(\mathbf{r}, t, M^2, \mathbf{p}) N(\mathbf{r}, t, M^2, \mathbf{p}) \quad (38)$$

as given by the off-shell test-particle approximation [Eq. (5)]. The isometric plots in Fig. 11 show $F(M, t)$ for central collisions of $Ni + Ni$ at 1.8 A·GeV for antikaons stemming from baryon-baryon (BB) (r.h.s.) and πY reactions (l.h.s.), separately. It is seen from Fig. 11 that the initial distribution of antikaons is widely spread in invariant mass for both production channels and that – with the expanding nuclear system – the antikaons become practically on-shell for large times, i.e. when moving to 'free' space with the expanding fireball. In case of the BB production channel the initial spreading in mass also shows sizeable contributions for $M \geq 0.5$ GeV whereas for the πY flavor exchange reaction dominantly low mass antikaons are produced which are kinematically not allowed in case of 'free' antikaon masses. The energy – to get on-shell finally – stems from the collective expansion of the hadronic system.

5.1 K^\pm spectra at SIS energies

Since kaons couple only weakly to nucleons and are not absorbed at low energies their collisional width is rather small such that they may be treated on-shell to a good approximation as in Ref. [77]. We recall, that the production channel $N\Delta \rightarrow NK^+Y$, where Y denotes a hyperon, as well as the $\Delta\Delta \rightarrow K^+NY$ channel is not known experimentally and simple isospin factors as extracted from pion exchange [77] might not be appropriate. Though there are some efforts to resolve this uncertainty within extended boson exchange models [78], the latter models will hardly be tested experimentally. We note that the $N\Delta \rightarrow NK^+Y$ and $\Delta\Delta \rightarrow K^+NY$ cross sections employed in the transport models of Refs. [79, 80] are larger by factors of 2 - 3 than ours, which leads to higher K^+ (and hyperon) cross sections from nucleus-nucleus collisions in the 'free' scenario [7]. These cross sections are reduced again in Refs. [79, 80] by a repulsive kaon potential in order to achieve a better agreement with measured kaon cross sections.

In this work we do not address this particular question in more detail since only the kaon abundancies are of interest here due to the associated productions with hyperons $Y = \Lambda, \Sigma$. As mentioned above, the channel $\pi Y \rightarrow K^- N$ is expected to be dominant such that the transport calculations have to reproduce the (experimental) hyperon abundancy with sufficient accuracy. Since there are no explicit hyperon spectra available from nucleus-nucleus collisions at SIS energies, we will perform a detailed comparison to measured K^+ spectra (see below).

On the other hand, antikaons couple strongly to nucleons and thus achieve a large collisional width in the nuclear medium as demonstrated in Fig. 2. Accordingly, off-shell antikaons might be produced at far subthreshold energies (cf. Fig. 10), become asymptotically on-shell (cf. Fig. 11) and thus enhance the K^- yield. In fact, as shown in the model study in Ref. [41] the K^- yield might be enhanced up to a factor of 2 for $Ni + Ni$ at 1.8 A·GeV when including the antikaon off-shell propagation. However, in the latter study the off-shell transition rates $\pi Y \leftrightarrow K^- N$ had been extrapolated from the on-shell rates in free space which according to Figs. 5-8 should be questionable.

In the following we will show three different limits simultaneously in comparison to the experimental data: i) a calculation without any antikaon in-medium effects (denoted by 'free'), where the G -matrix elements at density $\rho = 0$ are adopted and the antikaon spectral function is taken as a δ -function on-mass shell; ii) a calculation using the G -matrix elements, spectral functions and potentials from a G -matrix calculation without pion dressing and iii) a calculation using the G -matrix elements, spectral functions and potentials from a G -matrix calculation with pion dressing. We mention, that we use only the G -matrix elements calculated at an average temperature $T = 70$ MeV and do not follow the change of these matrix elements with decreasing temperature T . Apart from the tremendous numerical effort to calculate the G -matrix additionally on a narrow grid in temperature T , the modifications with temperature are rather moderate or even small (cf. Ref. [38]), such that we discard this variation.

The actual K^\pm spectra for the systems $C + C$ at 1.8 A·GeV and $\theta_{cm} = (90 \pm 10)^\circ$, $Ni + Ni$ at 1.8 A·GeV and $\theta_{lab} = (44 \pm 4)^\circ$ and $Au + Au$ at 1.5 A·GeV and $\theta_{cm} = (90 \pm 10)^\circ$ are shown in Figs. 12-14 in comparison to the data from Refs. [81, 82, 83, 84]. The K^+ spectra are shown in the upper plots whereas the K^- spectra are displayed in the lower parts, respectively. In Figs. 12-14 the K^+ spectra are displayed for the full G -matrix calculations only, since the K^+ spectra are practically insensitive to the different limits addressed for the antikaons within the statistics of the transport calculations.

In case of $C + C$ (Fig. 12) the 'slope' T_0 of the K^+ spectrum, defined by

$$E \frac{d^3\sigma}{dp^3} \sim \exp\left(-\frac{E_{cm}}{T_0}\right), \quad (39)$$

is slightly underestimated when comparing the data at $\theta_{cm} = (90 \pm 10)^\circ$ with the calculations in the same angular bin (solid line). However, when averaging the calculated K^+ spectrum over the solid angle Ω in the center-of-mass system (dashed line) the experimental spectrum is well described in shape as well as absolute magnitude. This comparison demonstrates that the details of the double differential cross with respect to the kaon

kinetic energy in the cms, E_{cm}^{kin} , and angle Ω are not fully reproduced by the transport calculation, but the kaon abundancy and average spectrum compare reasonably well. Due to the associated production of hyperons (with kaons) we thus conclude that also the average hyperon abundancy and spectra should compare sufficiently well with experiment though explicit data are not available for the Λ and Σ spectra.

For $Ni + Ni$ at 1.8 A·GeV (Fig. 13) the slope of the K^+ spectrum as well as the K^+ abundancy is slightly too low for the calculations at $\theta_{lab} = (44 \pm 4)^\circ$ (solid line) in comparison to the data in the same angular range. Again a very satisfactory description is obtained in case of the angle averaged calculated spectrum (dashed line) as in case of the $C + C$ system in Fig. 12, such that the interpretation and conclusions drawn in the context of the latter system also hold for $Ni + Ni$ at 1.8 A·GeV. Furthermore, for $Au + Au$ at 1.5 A·GeV (Fig. 14) the K^+ multiplicity seems to be roughly in line for the spectra in the angular range $\theta_{cm} = (90 \pm 10)^\circ$ (solid line) as well as for the angular averaged spectra (dashed line) in comparison to the preliminary data from Ref. [84].

The KaoS [85] and FOPI Collaborations [86] have independently measured K^+ production in $Ni + Ni$ collisions at 1.93 A·GeV. In fact, their experimental results for the inclusive K^+ rapidity distributions agree quite well in the common region of acceptance in rapidity such that systematic experimental uncertainties are much better under control. In Fig. 15 we compare our calculated rapidity distributions for this system with the data from Ref. [85] for 'semi-central' collisions that correspond to impact parameter $b \leq 4.5$ fm. For $Ni + Ni$ at 1.93 A·GeV our calculations almost perfectly agree with the measured K^+ rapidity distribution since deviations in the double differential K^+ spectra with respect to momentum and angle do not show up any more in the rapidity distributions.

The K^+ spectra from our transport calculations thus are found to be in 'approximate' agreement with the data for the various systems, however, systematic uncertainties in the order of 30% in the K^+ (and associated hyperon abundancies) cannot be excluded. On the other hand, it is presently not clear if the different data sets are compatible with each other to a higher accuracy.

We now turn to the results for the K^- spectra (lower parts in Figs. 12-15). Whereas for the 'free' calculations (dashed lines) the experimental K^- spectra are substantially underestimated for $C + C$ and $Ni + Ni$ at 1.8 A·GeV (in line with the calculations in Ref. [7, 65]) the preliminary data for $Au + Au$ at 1.5 A·GeV in Fig. 14 appear to be described rather well in magnitude. Only the slope of the calculated K^- spectrum is slightly too hard in this limit. Surprisingly, the K^- rapidity distribution for semi-central collisions of $Ni + Ni$ at 1.93 A·GeV (Fig. 15) is underestimated only by less than a factor of 2 in the 'free' case. This result - on first sight - appears incompatible with the comparison displayed in Fig. 13 for $Ni + Ni$ at 1.8 A·GeV where the K^- spectra are underestimated on average by more than a factor of 4 in the 'free' case².

The calculated slope T_0 of the K^- spectrum is too high for the $C + C$ system, roughly compatible for $Ni + Ni$ at 1.8 A·GeV and slightly too high again for $Au + Au$ at 1.5 A·GeV

²According to private communication with the KaoS Collaboration the normalization of the K^- data for $Ni + Ni$ at 1.8 A·GeV is estimated to be too high by up to a factor of 2, which is on the lower level of the error bars quoted in Ref. [82].

in the 'free' scenario when compared to the data in Figs. 12-14. The G -matrix calculations including pion dressing (full lines with open triangles) for $C + C$ at $\theta_{cm} = 90^\circ \pm 10^\circ$ are approximately compatible in magnitude with the 'free' calculations for kinetic energies above 100 MeV, however, the slope of the spectrum is now in better agreement with the data. For $Ni + Ni$ at 1.8 A·GeV and $\theta_{lab} = 44^\circ \pm 4^\circ$ the G -matrix calculations even fall slightly below the 'free' result whereas for $Au + Au$ at 1.5 A·GeV they are again compatible with the data and the 'free' result within statistics for $E_{kin}^{cm} > 100$ MeV. This also holds for the K^- rapidity distribution for $Ni + Ni$ at 1.93 A·GeV in Fig. 15 where the full G -matrix calculations reproduce the experimental spectrum almost 'perfectly'.

In general, the medium modifications of the K^- spectra are found to be only minor within the G -matrix calculations including pion dressing in the regime of antikaon momenta p_{cm} or kinetic energies E_{cm}^{kin} , where explicit data are available. This is surprising since the antikaon spectral functions show a sizeable shift of strength to lower invariant masses (Fig. 3) such that - according to phase-space - the cross sections should be enhanced. However, this expectation is only valid if the transition and production amplitudes do not change in the medium, which actually does not hold for the present G -matrix calculations as seen from Figs. 5-8. Accordingly, the dominant production channel $\pi + Y \rightarrow \bar{K}N$ decreases strongly with nuclear density due to the rapid melting of the $\Lambda(1405)$ and $\Sigma(1385)$ resonances with density such that less s -quarks now can be transferred from hyperons to antikaons at high baryon density. Qualitatively, our findings are similar to the self-consistent results of Ref. [37].

The relative role of the hyperon 'resonances' becomes more clear when looking at the results for the G -matrix calculations without pion dressing (solid lines with open circles in Figs. 12-15). In this case all spectra are found to be enhanced relative to the 'free' calculations and the G -matrix calculations with pion dressing. The experimental spectra for $C + C$ at $\theta_{cm} = 90^\circ \pm 10^\circ$ are still underestimated as well as for $Ni + Ni$ at 1.8 A·GeV and $\theta_{lab} = 44^\circ \pm 4^\circ$. However, the calculations for $Au + Au$ at 1.5 A·GeV and $Ni + Ni$ at 1.93 A·GeV now are clearly above the measured data. In line with the higher K^- multiplicity also the spectral slope softens slightly because the antikaon spectral strength is shifted to lower invariant masses in case of the 'surviving' subthreshold resonances $\Lambda(1405)$ and $\Sigma(1385)$, respectively. We argue, that the calculations with and without pion dressing represent a 'band of uncertainty' within the G -matrix calculations, that implicitly depend on the interaction schemes involved. Nevertheless, in all limits considered here there is no convincing description of all spectra simultaneously!

The question thus arises if medium effects for antikaons show up in kinematical regimes not accessible to the present detector setups. To this aim we show in Fig. 16 the Lorentz invariant K^- spectra for $C + C$ and $Ni + Ni$ at 1.8 A·GeV and $Au + Au$ at 1.5 A·GeV as a function of the antikaon momentum p_{cm} in the cms frame. Whereas above ~ 0.5 GeV/c all spectra within the limits addressed before are roughly comparable, a large enhancement at low momenta is found for all systems within the G -matrix calculations relative to the 'free' case. This enhancement is even more pronounced when excluding pion dressing (full lines with open circles). The K^- enhancement at low momenta is essentially due to a deceleration of antikaons in the combined attractive Coulomb and

nuclear mean field as well as due to the off-shell propagation of 'low mass' antikaons. In the off-shell propagation (see Eqs. (6)-(8)) spectral components with masses below the free pole mass (cf. Fig. 11) decrease in momentum during the expansion phase according to Eq. (7) in order to become on-shell in free space.

The results from Fig. 16, which qualitatively agree with the earlier analysis by Wang et al. [87] using on-shell transport calculations, also explain to some extent why the calculations within the full G -matrix approach are compatible with the K^- rapidity spectra for $Ni + Ni$ at 1.93 A·GeV (Fig. 15), that experimentally have been obtained by extrapolation to low antikaon momenta, but not with the K^- spectra for $Ni + Ni$ at 1.8 A·GeV (Fig. 13) in the higher momentum range of the KaoS acceptance. The reason is most likely related to the strong increase of the antikaon spectrum at low momenta in the cms.

5.2 K^-/K^+ ratios versus centrality

We continue with the K^-/K^+ ratio in $Au + Au$ collisions at 1.5 A·GeV as a function of centrality which has been also addressed experimentally by the KaoS Collaboration [84]. In Fig. 17 we show this ratio as a function of the number of participating nucleons A_{part} for the three limits discussed before including a cut $p_{cm} > 0.35$ GeV/c which roughly corresponds to the acceptance of the KaoS spectrometer in Ref. [84]. In the 'free' calculations as well as G -matrix calculations without pion dressing this ratio – within statistics – increases with centrality or A_{part} . This increase is no longer present for the G -matrix calculations with pion dressing (full line with open triangles). The preliminary data for this ratio from the KaoS Collaboration [84] (full circles) show - within errorbars - a slight decrease with A_{part} or an approximately constant value of $\sim 2\%$. This experimental value is not compatible with the G -matrix calculation excluding pion dressing as well as the 'free' calculation, however, in the order of the full G -matrix results.

Some comments on the K^-/K^+ ratio appear necessary since the dependence on centrality and its actual values strongly correlate with the angle and momentum cut introduced. This comes about because the K^- spectra show a softer slope in the momentum spectrum relative to the K^+ mesons, which we address to attractive in-medium effects for the antikaons. An alternative or complementary interpretation persists in relating the different slopes to different 'freeze-out' times since K^+ mesons decouple early in view of their low cross section with baryons, whereas antikaons interact strongly up to rather low densities of the expanding hadronic fireball. Consequently the relative change of the K^- to K^+ spectral slopes with centrality strongly affect the K^-/K^+ ratio in Fig. 17 (for a high momentum cut) such that no 'simple' interpretation can be drawn directly. Without explicit representation we mention that in our calculations the K^-/π^- and K^+/π^+ ratios increase both with centrality (or A_{part}). However, also the difference in the slopes for K^+ and K^- mesons increases with A_{part} for the full G -matrix calculations including pion dressing.

5.3 K^\pm angular distributions

We finally come to the K^\pm angular distributions in the cms for $Au + Au$ collisions at 1.5 A·GeV that also have been measured by the KaoS Collaboration [88] for two different centrality cuts. In Fig. 18 we show these angular distributions for the three limits discussed before for K^- mesons (lower part), whereas the angular distributions for K^+ mesons (upper part) are shown for the full G -matrix calculations, only, since the same distribution has been obtained in the three limits (within statistics). All angular distributions are normalized to unity for $\cos\theta_{cm} = 0$.

We see that the K^+ angular distributions from our calculations for semi-central ($b < 6$ fm) and non-central ($b > 6$ fm) collisions are more isotropic than the data. This points towards a lower amount of K^+ rescattering in the data [88] especially for non-central collisions. On the other hand, all three limits are compatible with the experimental measurements for K^- -mesons in semi-central reactions, which are roughly compatible with an isotropic distribution within statistics. Differences appear only for non-central reactions, where the 'free' (dashed line) and G -matrix calculation without pion dressing (solid line with open circles) are closer to isotropy while the full G -matrix calculations with pion dressing (solid lines with open triangles) show a distribution, that is forward-backward peaked in the cms in better agreement with the data. We attribute this result to the lower amount of s -quark exchange reactions in the full G -matrix calculations (cf. Section 3).

6 Summary

In this work we have studied the production and propagation of antikaons with dynamical spectral functions $A_h(X, \vec{P}, M^2)$ using off-shell transport theory. The in-medium properties of the antikaons have been determined in a coupled-channel G -matrix approach including elastic scattering, charge exchange and s -quark exchange reactions with baryons. Antikaon mean-field potentials as well as spectral properties are uniquely determined within the G -matrix approach. However, the actual results strongly depend on the many-body scheme involved, especially on the dressing of the pions. Though in all cases the spectral strength of the antikaon is shifted to lower invariant masses with increasing density, we find that, when including pion self energies, the $\Lambda(1405)$ and $\Sigma(1385)$ resonance structures in the transition probabilities melt away with baryon density already at $\sim 0.25 \rho_0$. This implies that K^- absorption as well as production from pion-hyperon collisions should be strongly suppressed in nuclear media as produced in nucleus-nucleus collisions at SIS energies (1–2 A·GeV) or even proton-nucleus reactions at 2–3 GeV [89].

From our dynamical calculations we find that the experimental K^- spectra for $^{12}C + ^{12}C$ and $^{58}Ni + ^{58}Ni$ are underestimated in the 'free' as well as full G -matrix transport approach whereas the preliminary spectra for $Au + Au$ at 1.5 A·GeV are rather well described in case of calculations without any medium effects as well as with all medium effects included. The dominant medium effect is a 'softening' of the antikaon spectra which is more in line with the data. Furthermore, the full in-medium calculations agree

very well with the K^- rapidity spectra for semi-central collisions of $Ni+Ni$ at 1.93 A·GeV while the spectra are underestimated by up to a factor of 2 for 'free' transition matrix elements and spectral functions. In addition, the centrality dependence of the K^-/K^+ ratio for $Au + Au$ reactions at 1.5 A·GeV is rather well in line with the preliminary data of the KaoS collaboration for our full G -matrix calculations including pion dressing. The latter limit also provides the best description for the K^- angular distributions in the cms, especially for non-central $Au + Au$ reactions at 1.5 A·GeV (Fig. 18), which we interpret as a consequence of the lower amount of s -quark exchange reactions in the full G -matrix calculations.

Nevertheless, in all limits considered in this work there is no convincing description of all spectra simultaneously. This failure might be either attributed to larger systematic errors in the experimental data – as found for K^+ production in $p + A$ reactions from 1–2.5 GeV [90] – or to an inadequacy of the many-body schemes adopted for the coupled-channel G -matrix calculations, especially the 'pion dressing'. Additionally, there is no direct experimental test of the hyperon dynamics incorporated in the off-shell transport approach since no explicit hyperon spectra are available for the systems measured at the SIS accelerator. These issues can only be settled by new experimental data in a wider kinematical regime with emphasis on low antikaon momenta in the center-of-mass frame since the in-medium effects are found to be most pronounced in this region as established experimentally also in K^+ production from $p + A$ reactions for bombarding energies from 1-2 GeV [91].

The authors like to thank M. Lutz for stimulating discussions and P. Senger for valuable comments on the manuscript. L.T. wishes to acknowledge the hospitality extended to her at the Institut für Theoretische Physik (Universität Giessen). This work is also partly supported by the DGICYT project BFM2002-01868 and by the Generalitat de Catalunya project SGR 2001-64.

References

- [1] Z. Fodor and S. D. Katz, Phys. Lett. B 534 (2002) 87.
- [2] C. R. Allton, S. Ejiri, S. J. Hands, O. Kaczmarek, F. Karsch, E. Laermann, and C. Schmidt, *hep-lat/0305007*.
- [3] D. B. Kaplan and A. E. Nelson, Phys. Lett. B 175 (1986) 57.
- [4] A.E. Nelson and D. Kaplan, Phys. Lett. B 192 (1987) 193.
- [5] J. Schaffner-Bielich, I. N. Mishustin and J. Bondorf, Nucl. Phys. A 625 (1997) 325.
- [6] S. J. Dong, J. F. Lagae, and K. F. Liu, Phys. Rev. D 54 (1996) 5496.
- [7] W. Cassing and E. L. Bratkovskaya, Phys. Rep. 308 (1999) 65.

- [8] G.-Q. Li, C. M. Ko, and X. S. Fang, Phys. Lett. B 329 (1994) 149.
- [9] J. Schaffner, A. Gal, I. N. Mishustin, H. Stöcker, and W. Greiner, Phys. Lett. B 334 (1994) 268.
- [10] T. Maruyama, H. Fujii, T. Muto, and T. Tatsumi, Phys. Lett. B 337 (1994) 19.
- [11] G. E. Brown, C. M. Ko, Z. G. Wu, and L. H. Xia, Phys. Rev. C 43 (1991) 1881.
- [12] T. Muto, Nucl. Phys. A 691 (2001) 447.
- [13] P. K. Sahu and A. Ohnishi, Nucl. Phys. A 691 (2001) 439.
- [14] A. Ramos, J. Schaffner-Bielich, and J. Wambach, Lectures Notes in Physics 578 (2001) 175, and references therein.
- [15] C. M. Ko, J. Phys. G 27 (2001) 327.
- [16] G. Q. Li, C.-H. Lee and G. E. Brown, Nucl. Phys. A 625 (1997) 372.
- [17] S. Pal, C. M. Ko, and Z.-W. Lin, Phys. Rev. C 64 (2001) 042201.
- [18] F. Laue et al., Phys. Rev. Lett. 82 (1999) 1640.
- [19] C. Sturm et al., Phys. Rev. Lett. 86 (2001) 39.
- [20] G. E. Brown and M. Rho, Phys. Rev. Lett. 66 (1991) 2720.
- [21] M. Lutz and E. E. Kolomeitsev, Nucl. Phys. A700 (2002) 193.
- [22] B. Krippa, Phys. Rev. C 58 (1998) 1333.
- [23] D. Jido, E. Oset, and A. Ramos, Phys. Rev. C 66 (2002) 055203.
- [24] A. Sibirtsev and W. Cassing, Nucl. Phys. A 641 (1998) 476.
- [25] E. Friedman, A. Gal, and C.J. Batty, Nucl. Phys. A 579 (1994) 518.
- [26] A. Gal, Nucl. Phys. A 691 (2001) 268.
- [27] M. Lutz, Phys. Lett. B 426 (1998) 12.
- [28] A. Ramos and E. Oset, Nucl. Phys. A 671 (2000) 481.
- [29] L. Tolós, A. Ramos, A. Polls, and T.T.S. Kuo, Nucl. Phys. A 690 (2001) 547.
- [30] E. Oset and A. Ramos, Nucl. Phys. A 635 (1998) 99.
- [31] S. Hirenzaki, Y. Okumura, H. Toki, E. Oset, and A. Ramos, Phys. Rev. C 61 (2000) 055205.

- [32] A. Ramos, S. Hirenzaki, S. S. Kamalov, T.T.S. Kuo, Y. Okumura, E. Oset, A. Polls, H. Toki, and L. Tolos, Nucl. Phys. A 691 (2001) 259.
- [33] A. Baca, C. García-Recio, and J. Nieves, Nucl. Phys. A 673 (2000) 335.
- [34] A. Cieplý, E. Friedman, A. Gal, and J. Mareš, Nucl. Phys. A 696 (2001) 173.
- [35] N. Kaiser, P.B. Siegel, and W. Weise, Nucl. Phys. A 594 (1995) 325; N. Kaiser, T. Waas, and W. Weise, Nucl. Phys. A 612 (1997) 297.
- [36] C. García-Recio, A. J. Melgarejo, and J. Nieves, Phys. Rev. C 67 (2003) 047601.
- [37] J. Schaffner-Bielich, V. Koch, and M. Effenberger, Nucl. Phys. A 669 (2000) 153.
- [38] L. Tolós, A. Ramos, and A. Polls, Phys. Rev. C 65 (2002) 054907.
- [39] M. Lutz and C. L. Korpa, Nucl. Phys. A 700 (2002) 309.
- [40] W. Cassing and S. Juchem, Nucl. Phys. A 665 (2000) 377.
- [41] W. Cassing and S. Juchem, Nucl. Phys. A 672 (2000) 417.
- [42] W. Cassing and S. Juchem, Nucl. Phys. A 677 (2000) 445.
- [43] L. P. Kadanoff and G. Baym, *Quantum statistical mechanics*, Benjamin, New York, 1962.
- [44] P. Danielewicz, Ann. Phys. (NY) 152 (1984) 305.
- [45] S. Leupold, Nucl. Phys. A 672 (2000) 475; Nucl. Phys. A 695 (2001) 377.
- [46] Yu. B. Ivanov, J. Knoll, and D. N. Voskresensky, Nucl. Phys. A 672 (2000) 313.
- [47] Yu. B. Ivanov, J. Knoll, H. van Hees, and D. N. Voskresensky, Yad. Fiz. 64 (2001) 711.
- [48] Yu. B. Ivanov, J. Knoll, and D. N. Voskresensky, Ann. Phys. (NY) 293 (2001) 126.
- [49] Yu. B. Ivanov, J. Knoll, and D. N. Voskresensky, *nucl-th/0303006*, Phys. Atom. Nucl. (2003), in print.
- [50] W. Botermans and R. Malfliet, Phys. Rep. 198 (1990) 115.
- [51] A. Müller-Groeling, K. Holinde, and J. Speth, Nucl. Phys. A 513 (1990) 557.
- [52] E. Oset and W. Weise, Nucl. Phys. A 319 (1979) 477
- [53] E. Oset, H. Toki and W. Weise, Phys. Reports 83 (1982) 281
- [54] W.H. Dickhoff, A. Faessler, J. Meyer-ter-Vehn and H. Müther, Phys. Rev. C 23 (1981) 1154

- [55] W.H. Dickhoff, A. Faessler, J. Meyer-ter-Vehn and H. Müther, Nucl. Phys. A 368 (1981) 445
- [56] W.H. Dickhoff, Nucl. Phys. A 405 (1983) 534
- [57] S. Babu and G.E. Brown, Ann. of Phys. 78 (1973) 1
- [58] H.C. Chiang, E. Oset and P. Fernandez de Cordoba, Nucl. Phys. A 510 (1990) 591
- [59] R.C. Carrasco, E. Oset and L.L. Salcedo, Nucl. Phys. A 541 (1992) 585
- [60] C. Garcia-Recio, E. Oset, L.L. Salcedo, D. Strottman and M.J. Lopez, Nucl. Phys. A 526 (1991) 685
- [61] R.C. Carrasco and E. Oset, Nucl. Phys. A 565 (1993) 797
- [62] H. Schopper (Editor), Landolt-Börnstein, New Series, Vol. I/12, Springer-Verlag, 1988.
- [63] C.-H. Lee, D.-P. Min and M. Rho, Nucl. Phys. A 602 (1996) 334.
- [64] B. V. Krippa and J. T. Londergan, Phys. Rev. C 58 (1998) 1634.
- [65] W. Cassing, E.L. Bratkovskaya et al., Nucl. Phys. A 614 (1997) 415.
- [66] C. Hartnack, H. Oeschler, and J. Aichelin, Phys. Rev. Lett. 90 (2003) 102302.
- [67] W. Ehehalt and W. Cassing, Nucl. Phys. A 602 (1995) 449.
- [68] H. Weber, E. L. Bratkovskaya, W. Cassing, and H. Stöcker, Phys. Rev. C 67 (2003) 014904.
- [69] A. Sibirtsev and W. Cassing, *nucl-th/9904046*.
- [70] J. T. Balewski et al., Phys. Lett. B 420 (1998) 211
- [71] P. Moskal et al., Phys. Lett. B 482, 356 (2000).
- [72] E. Bycking and K. Kajantie, *Particle Kinematics*, John Wiley and Sons, 1973.
- [73] S. Teis et al., Phys. Rev. C50 (1994) 388.
- [74] A. Sibirtsev, W. Cassing, G. I. Lykasov, and M. V. Rzjanin, Nucl. Phys. A 632 (1998) 131.
- [75] C. Caso et al., (Review of Particle Properties), Eur. Phys. J. C 15 (2000) 1.
- [76] W. Cassing and E. L. Bratkovskaya, Nucl. Phys. A 623 (1997) 570.
- [77] E. L. Bratkovskaya, W. Cassing and U. Mosel, Nucl. Phys. A 622 (1997) 593.

- [78] K. Tsushima, A. Sibirtsev, and A. W. Thomas, *Phys. Rev. C* 59 (1999) 369.
- [79] C. Hartnack and J. Aichelin, *J. Phys. G* 28 (2002) 1649.
- [80] G. Q. Li, C.-H. Lee, and G. E. Brown, *Nucl. Phys. A* 625 (1997) 372.
- [81] H. Oeschler, *J. Phys. G* 28 (2002) 1787.
- [82] R. Barth et al., *Phys. Rev. Lett.* 78 (1997) 4007.
- [83] A. Schröter et al., *Z. Phys. A* 350 (1994) 101.
- [84] A. Förster for the KaoS Collaboration, *J. Phys. G* 28 (2002) 2011.
- [85] M. Menzel et al., *Phys. Lett. B* 495 (2000) 26.
- [86] D. Best et al., *Nucl. Phys. A* 625 (1997) 307.
- [87] Z. S. Wang, A. Faessler, C. Fuchs, U. S. Uma Maheswari, and T. Waindzoeh, *Phys. Rev. C* 57 (1998) 3284.
- [88] A. Förster for the KaoS Collaboration, MESON 2002, Proc. of the 7th International Workshop on Production, Properties and Interactions of Mesons, ed. by L. Jarczyk et al., World Scientific, Singapore, 2003, p. 473.
- [89] W. Scheinast for the KaoS Collaboration, *Acta. Phys. Pol. B* 31 (2000) 2305.
- [90] Z. Rudy et al., *Eur. Phys. J. A* 15 (2002) 303.
- [91] M. Nekipelov et al., *Phys. Lett. B* 540 (2002) 207.

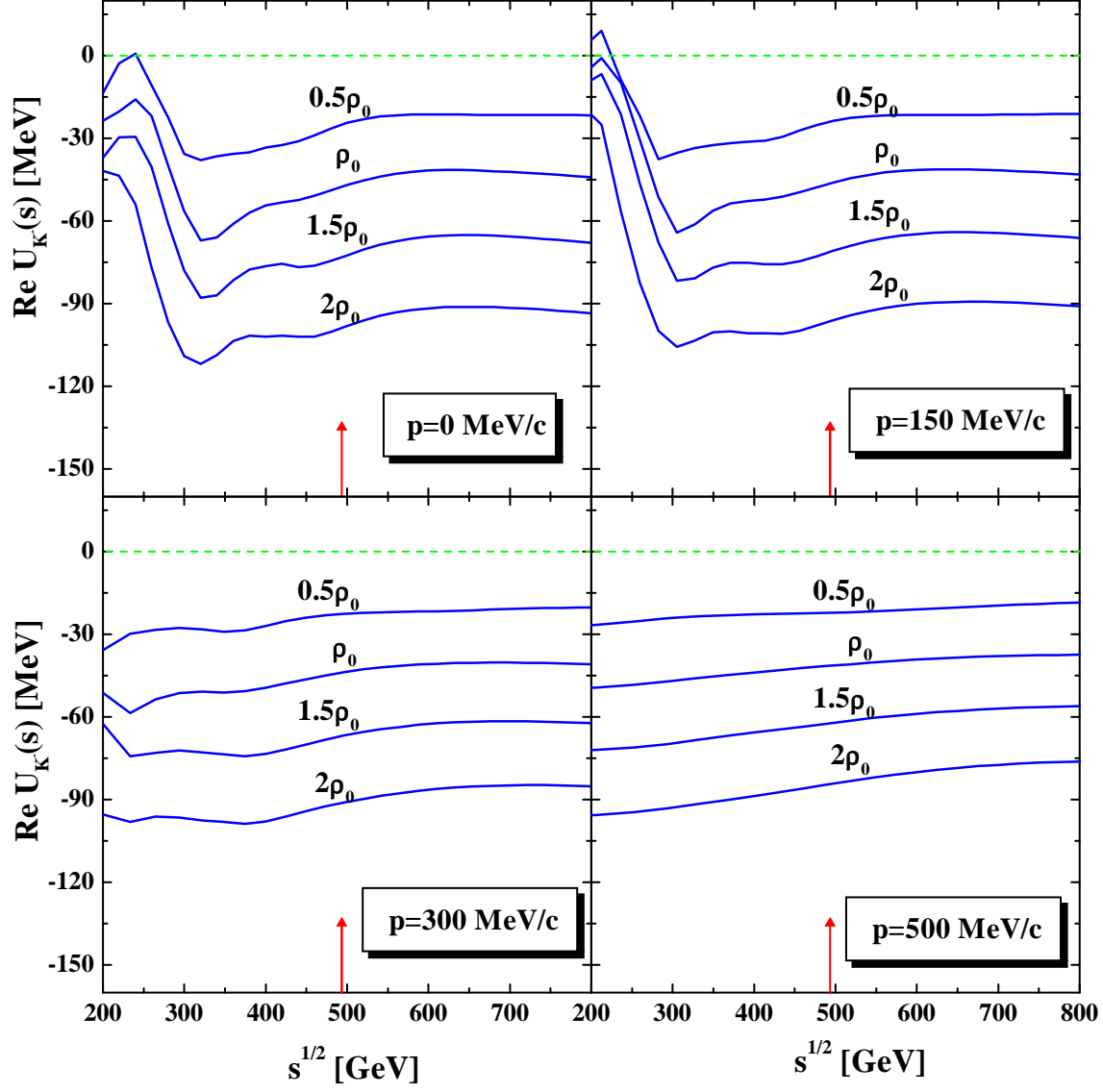


Figure 1: The real part of the antikaon potential $\text{Re } U_{\bar{K}}$ as a function of \sqrt{s} (Eq. (31)) for different nuclear densities and momenta $p_{\bar{K}} = 0, 150, 300,$ and 500 MeV/c, respectively. The arrows show the pole mass of the antikaon in free space.

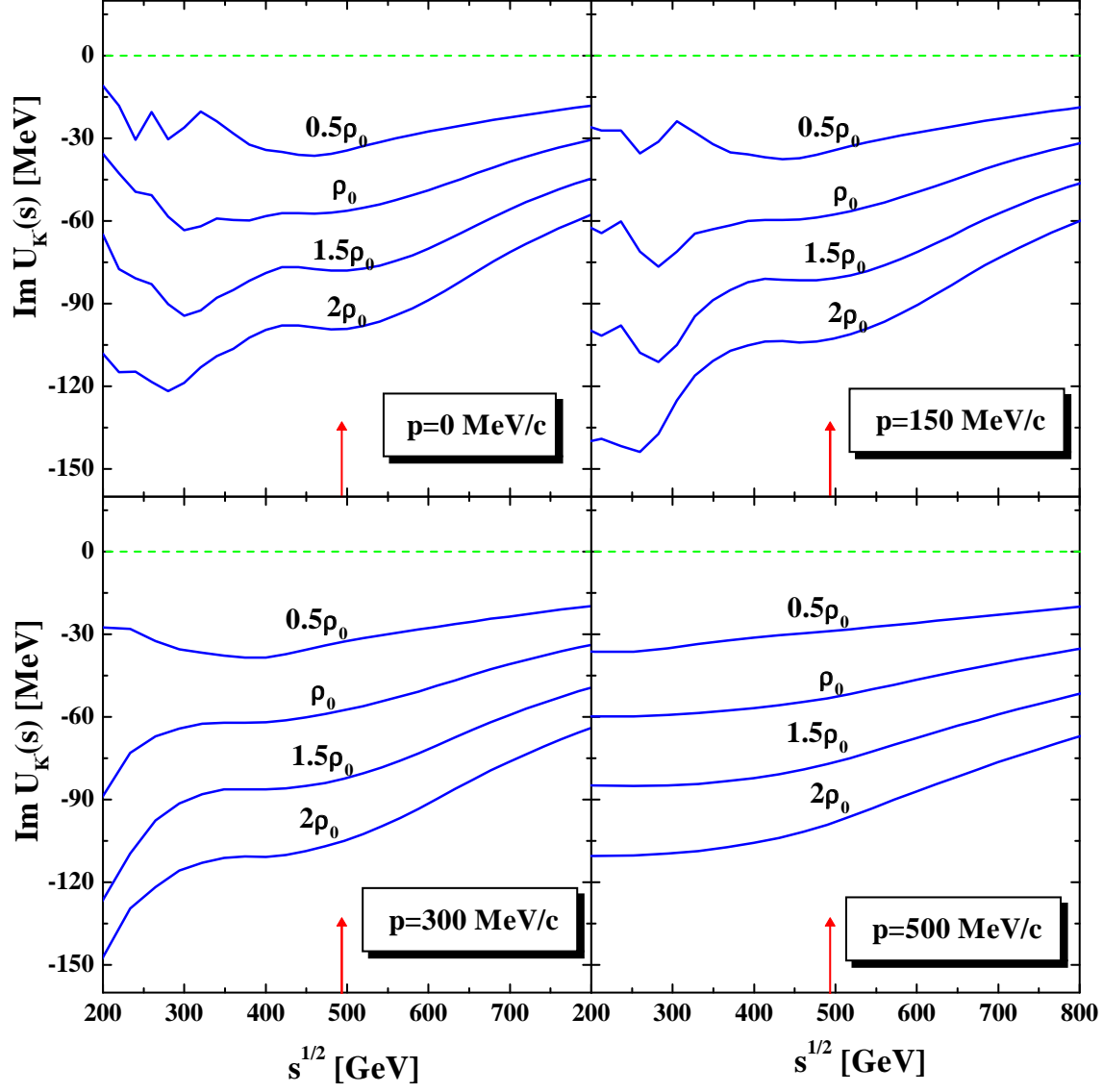


Figure 2: The imaginary part of the antikaon potential $\text{Im } U_{\bar{K}}$ as a function of \sqrt{s} (Eq. (31)) for different nuclear densities and momenta $p_{\bar{K}} = 0, 150, 300,$ and 500 MeV/c, respectively. The arrows show the pole mass of the antikaon in free space.

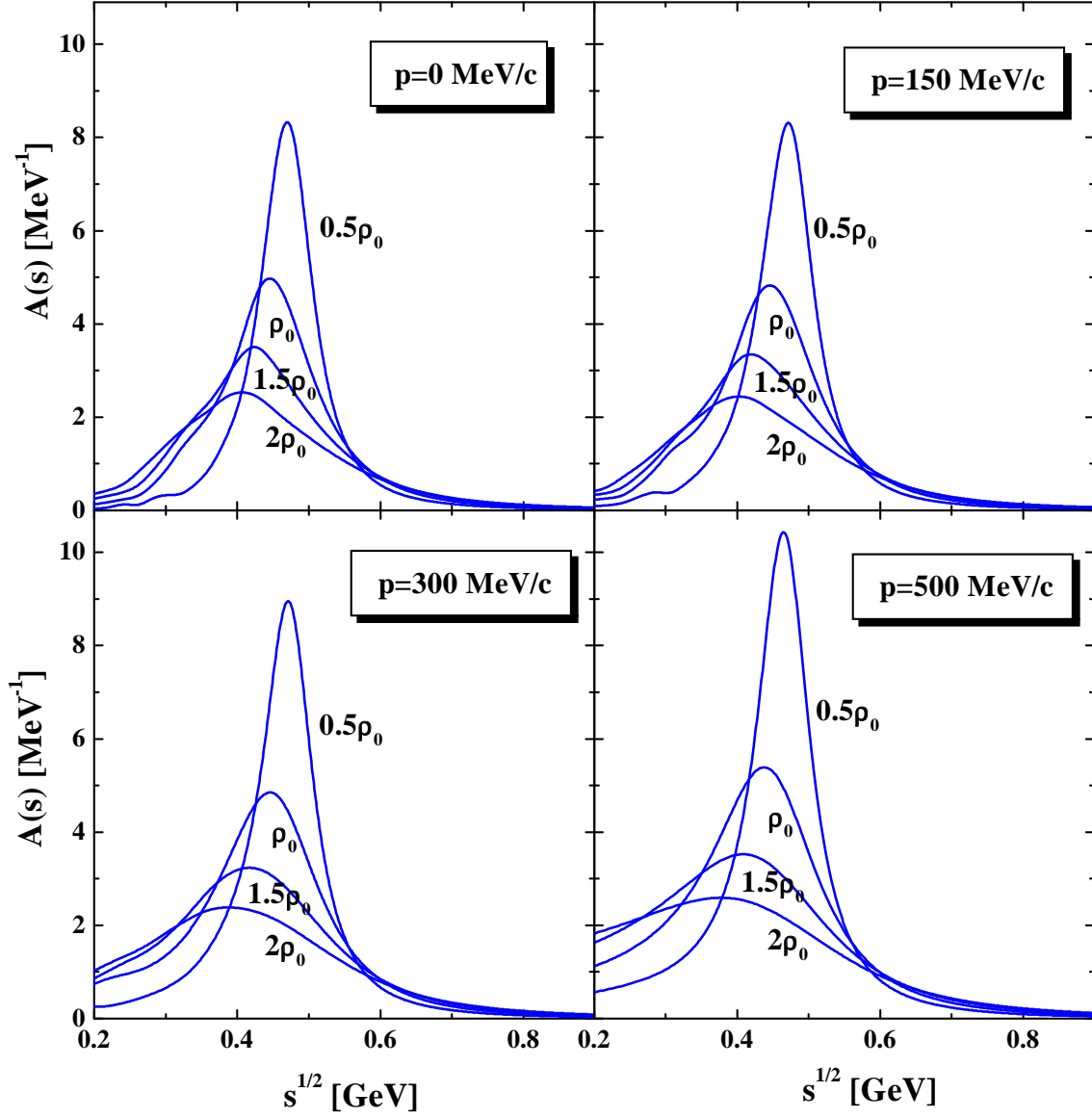


Figure 3: The antikaon spectral function $A(p_{\bar{K}}, \sqrt{s})$ (Eq. (32)) for different nuclear densities and momenta $p_{\bar{K}} = 0, 150, 300,$ and 500 MeV/c .

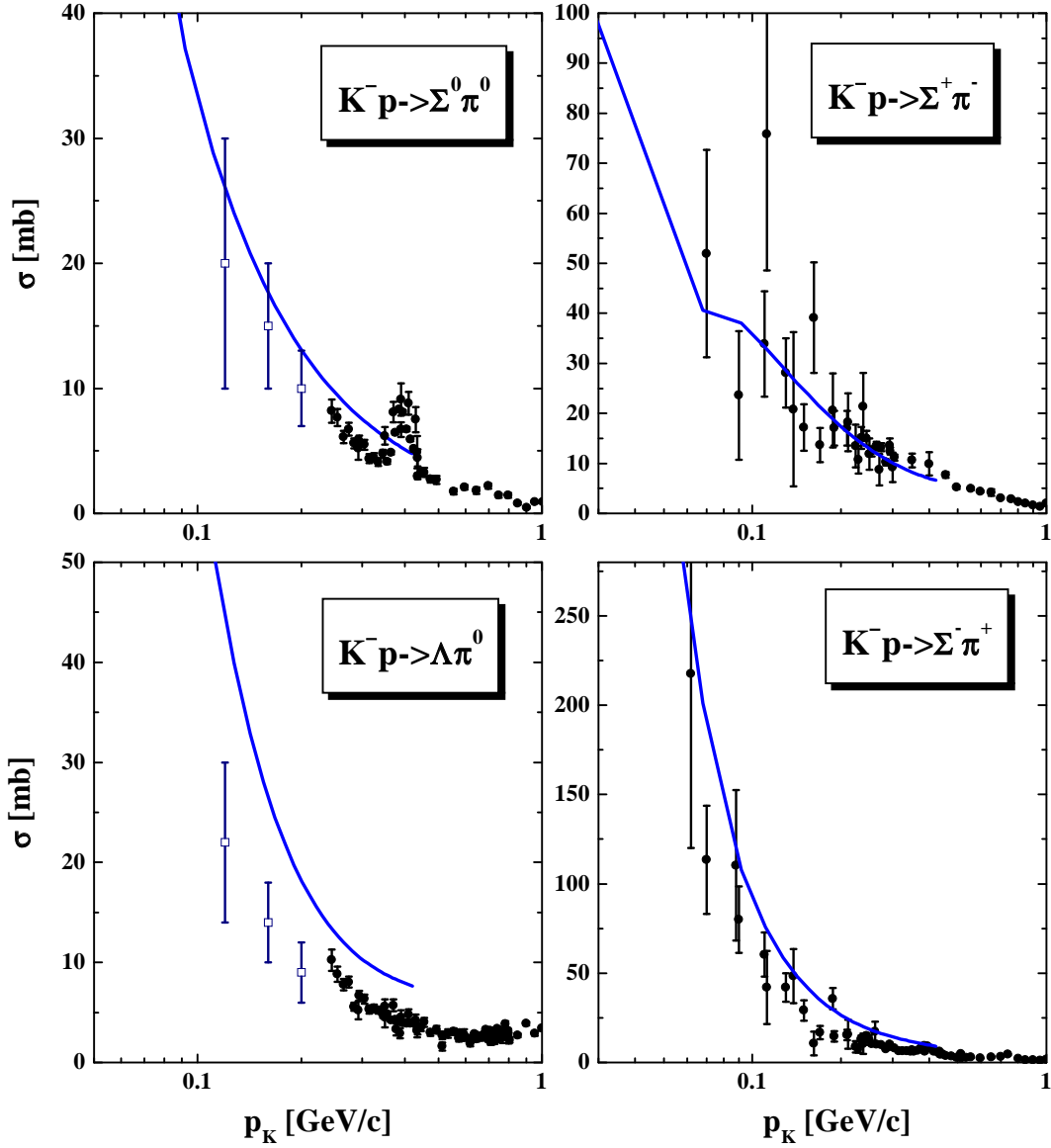


Figure 4: The K^-p cross sections to the final channels $\Sigma^0\pi^0$, $\Sigma^+\pi^-$, $\Sigma^-\pi^+$ and $\Lambda\pi^0$ according to the G -matrix calculations in 'free' space in comparison to the data from [62].

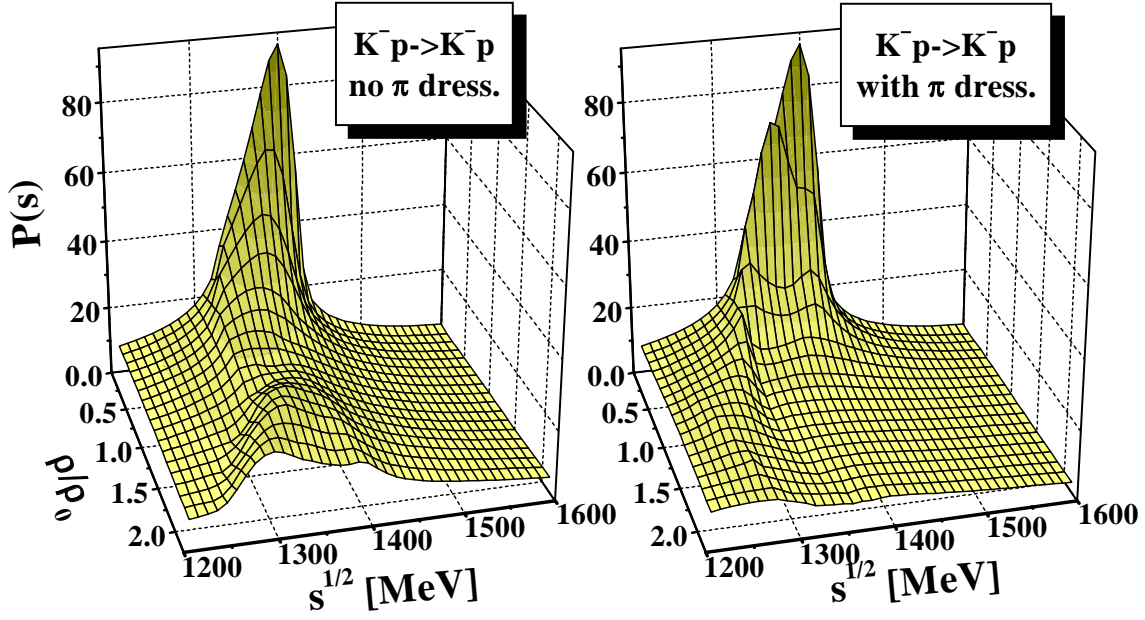


Figure 5: The transition probability $P_{1+2 \rightarrow 3+4}(s)$ (Eq. (34)) for the channel $K^- p \rightarrow K^- p$ as a function of \sqrt{s} and the nuclear density ρ (in units of ρ_0) for a momentum $p_{\bar{K}} = 0$ relative to the nuclear matter rest frame. The l.h.s. corresponds to a calculation without pion dressing whereas pion dressing is included in the G -matrix calculations of the r.h.s.

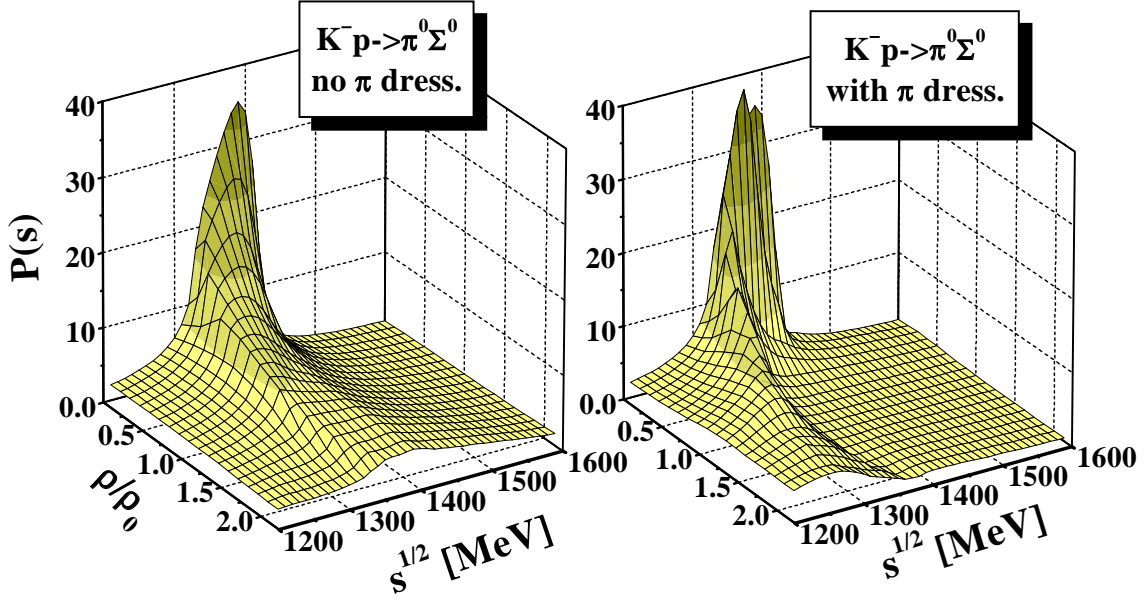


Figure 6: The transition probability $P_{1+2 \rightarrow 3+4}(s)$ (Eq. (34)) for the channel $K^- p \rightarrow \Sigma^0 \pi^0$ as a function of \sqrt{s} and the nuclear density ρ for a momentum $p_{\bar{K}} = 0$ relative to the nuclear matter rest frame. The l.h.s. corresponds to a calculation without pion dressing whereas pion dressing is included in the G -matrix calculations of the r.h.s.

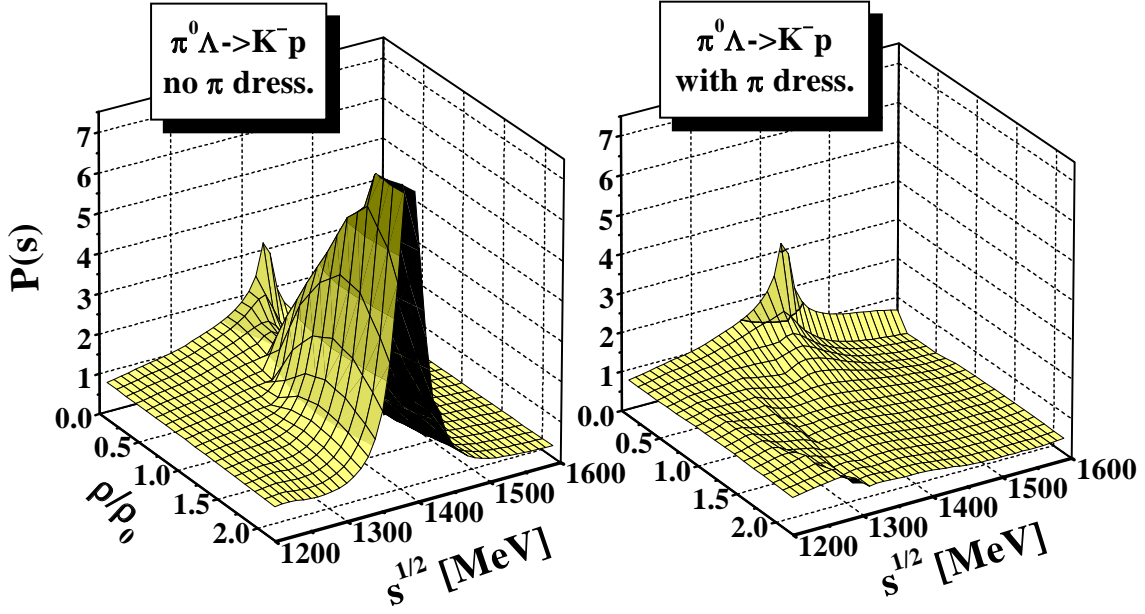


Figure 7: The transition probability $P_{1+2 \rightarrow 3+4}(s)$ (Eq. (34)) for the channel $\Lambda\pi^0 \rightarrow K^-p$ as a function of \sqrt{s} and the nuclear density ρ for a momentum $p_{\bar{K}} = 0$ relative to the nuclear matter rest frame. The l.h.s. corresponds to a calculation without pion dressing whereas pion dressing is included in the G -matrix calculations of the r.h.s.

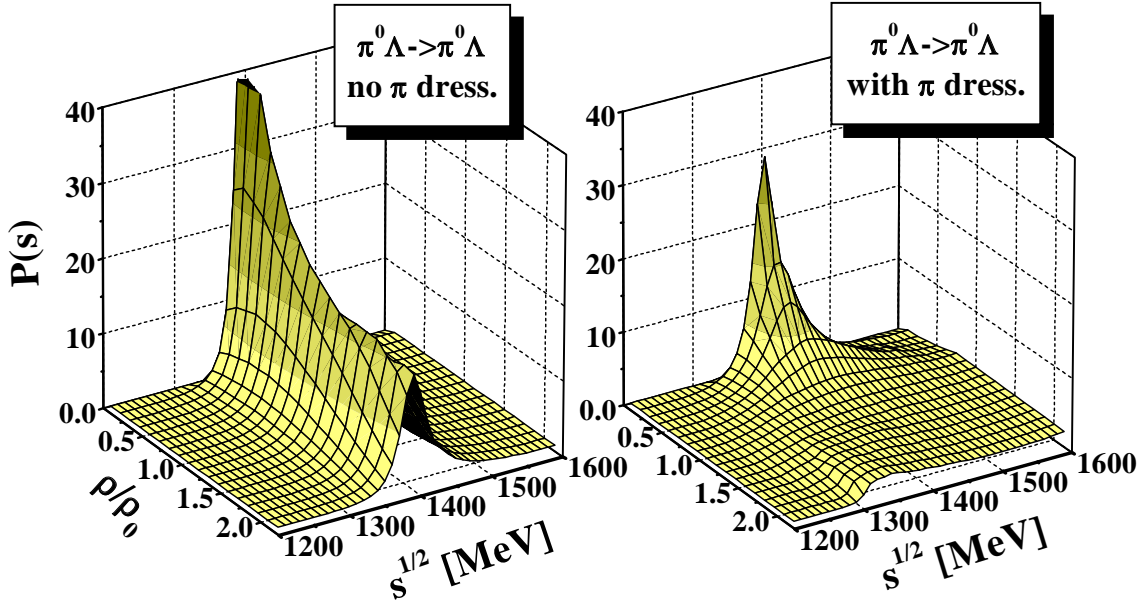


Figure 8: The transition probability $P_{1+2 \rightarrow 3+4}(s)$ (Eq. (34)) for the channel $\Lambda\pi^0 \rightarrow \Lambda\pi^0$ as a function of \sqrt{s} and the nuclear density ρ for a momentum $p_{\bar{K}} = 0$ relative to the nuclear matter rest frame. The l.h.s. corresponds to a calculation without pion dressing whereas pion dressing is included in the G -matrix calculations of the r.h.s.

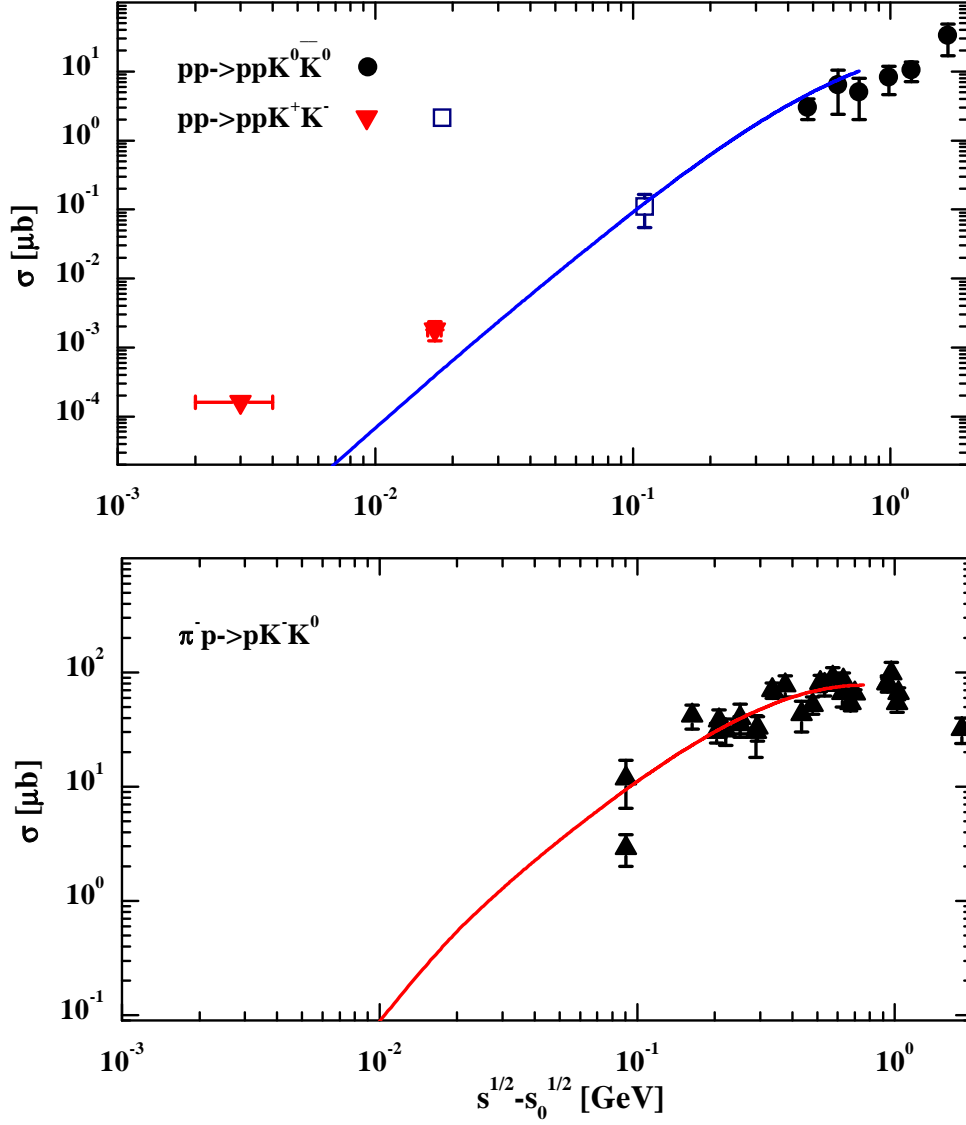


Figure 9: The experimental data for the reactions $pp \rightarrow K^0 \bar{K}^0 pp$, $pp \rightarrow K^+ K^- pp$ (from Refs. [70, 62, 71]) and $\pi^- p \rightarrow K^- K^0 p$ (from Ref. [62]) in comparison to our parametrizations (solid lines).

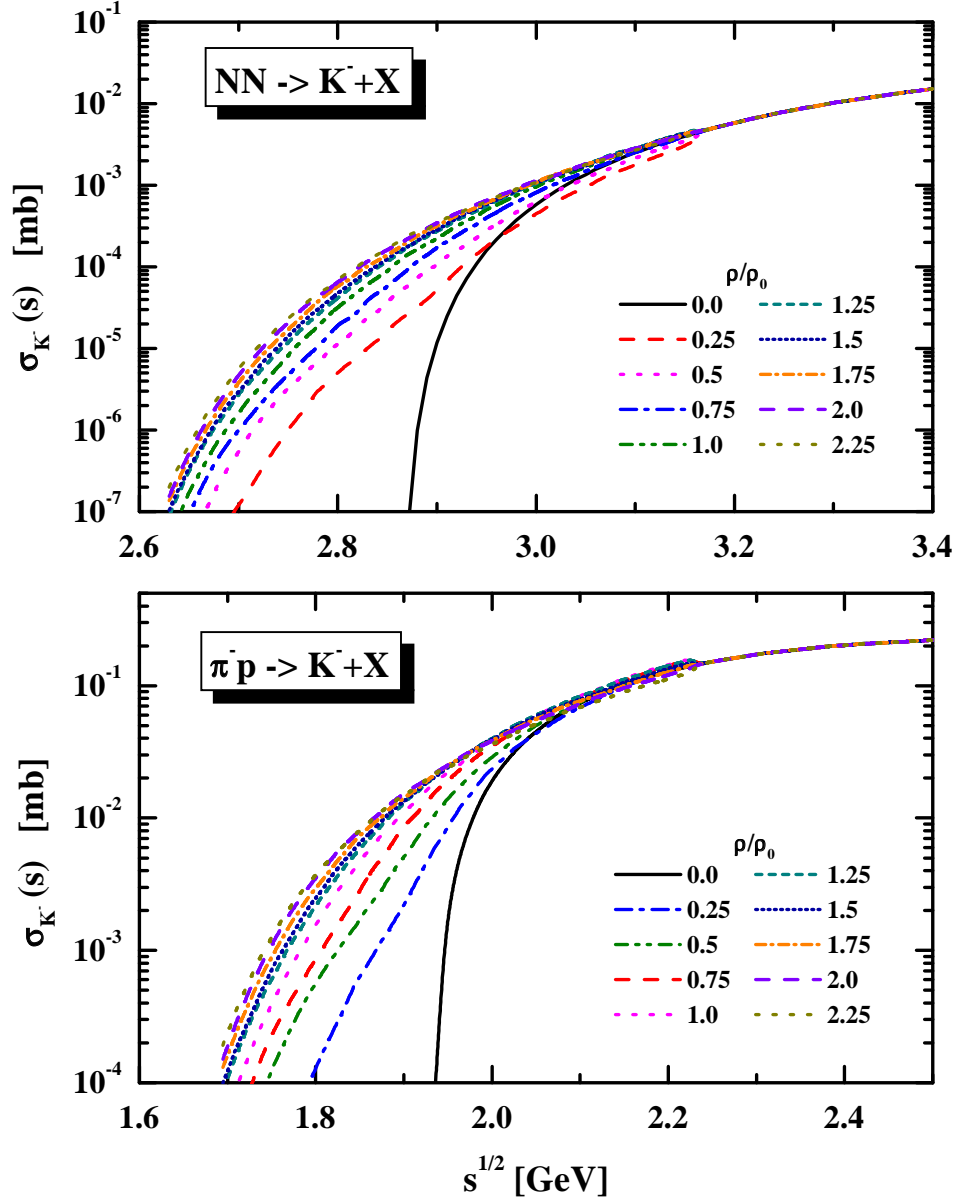


Figure 10: The in-medium cross sections for K^- production from NN and π^-p collisions for on-shell nucleons and kaons in the final state, however, employing the antikaon spectral functions from the G -matrix approach in Section 3 as a function of \sqrt{s} for different nuclear densities ranging from $0.25 \rho_0$ to $2.25 \rho_0$ in comparison to the cross section in free space (solid lines).

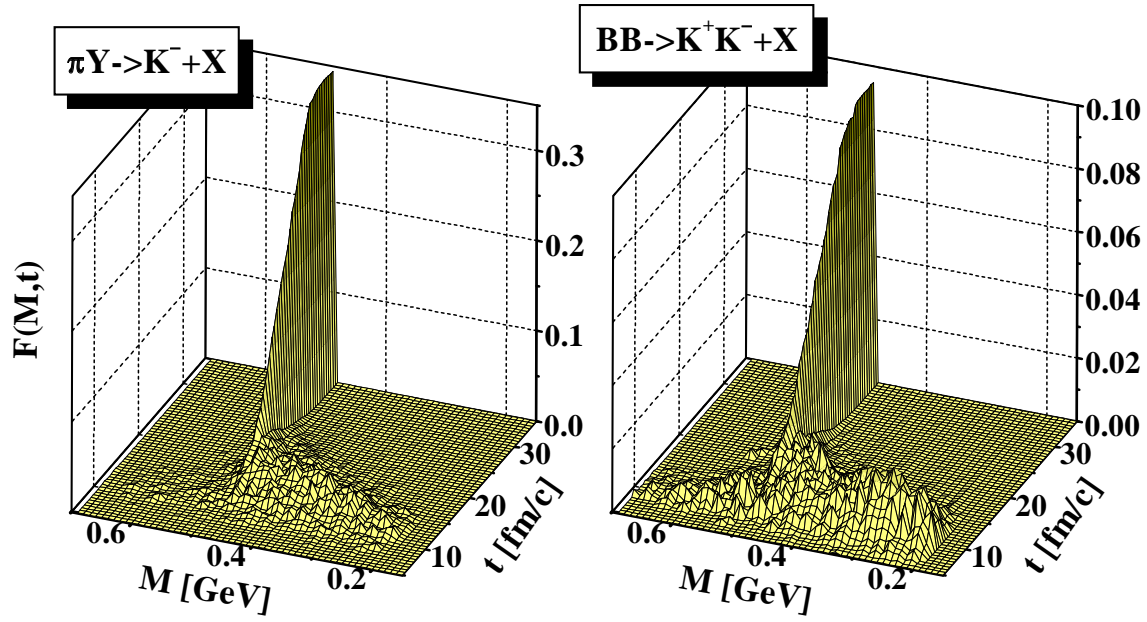


Figure 11: The time evolution of the antikaon spectral distribution (Eq. (38)) in central $Ni + Ni$ collisions at 1.8 A·GeV. The l.h.s. displays the antikaons stemming from the πY channel whereas the r.h.s. shows the antikaons emerging from baryon-baryon collisions.

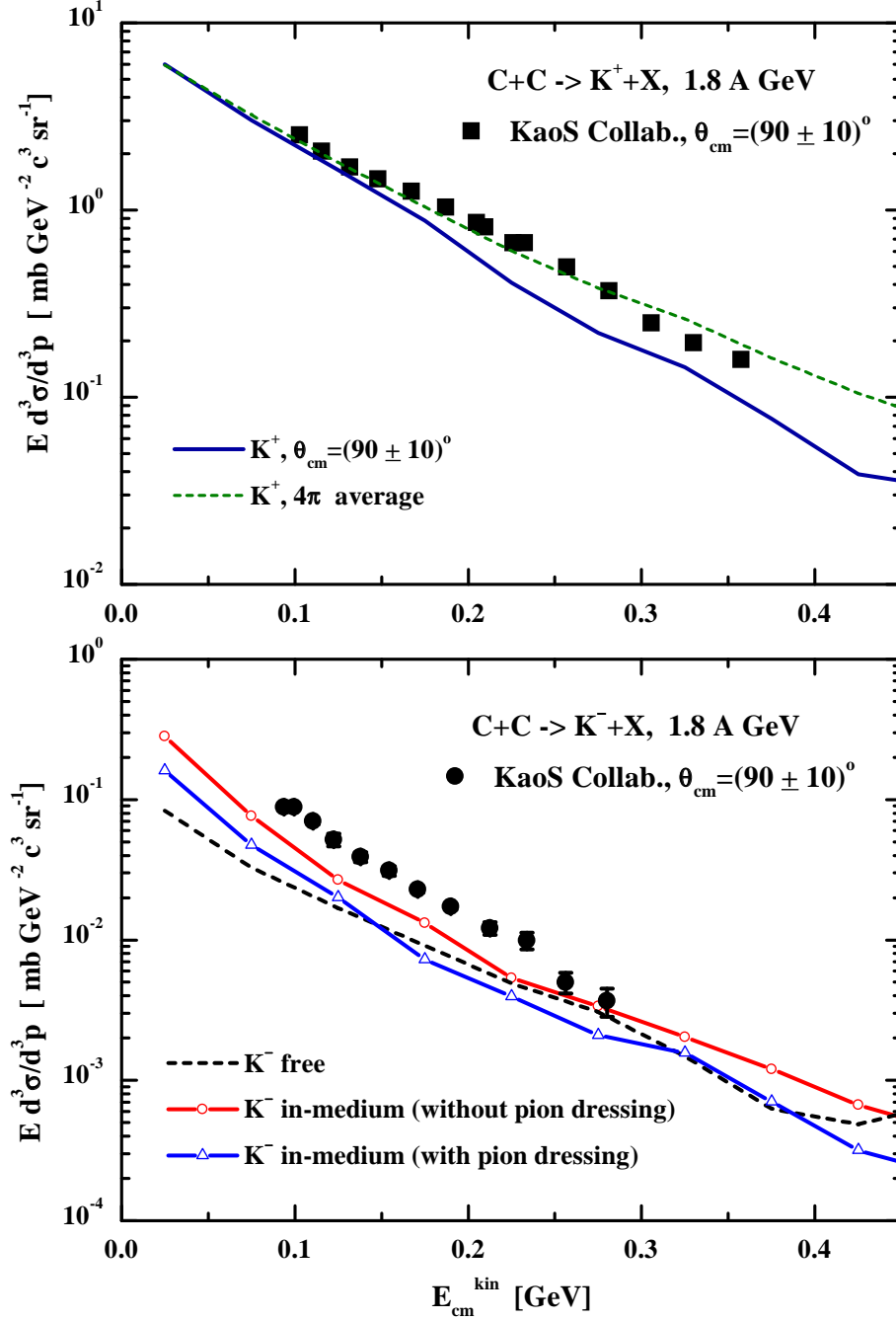


Figure 12: The differential inclusive K^+ (upper part) and K^- spectrum (lower part) for the system $C + C$ at $1.8 \text{ A} \cdot \text{GeV}$ and $\theta_{cm} = (90 \pm 10)^\circ$ in comparison to the data from Ref. [81]. The dashed line in the upper part reflects the result of the transport calculation after averaging the K^+ spectra over the angle Ω in the center-of-mass system, while the solid line displays the calculated spectrum for $\theta_{cm} = (90 \pm 10)^\circ$. Lower part: The dashed line corresponds to a 'free' calculation, the solid line with open triangles to a G -matrix calculation including pion dressing whereas the solid line with open circles results from a G -matrix calculation without pion dressing.

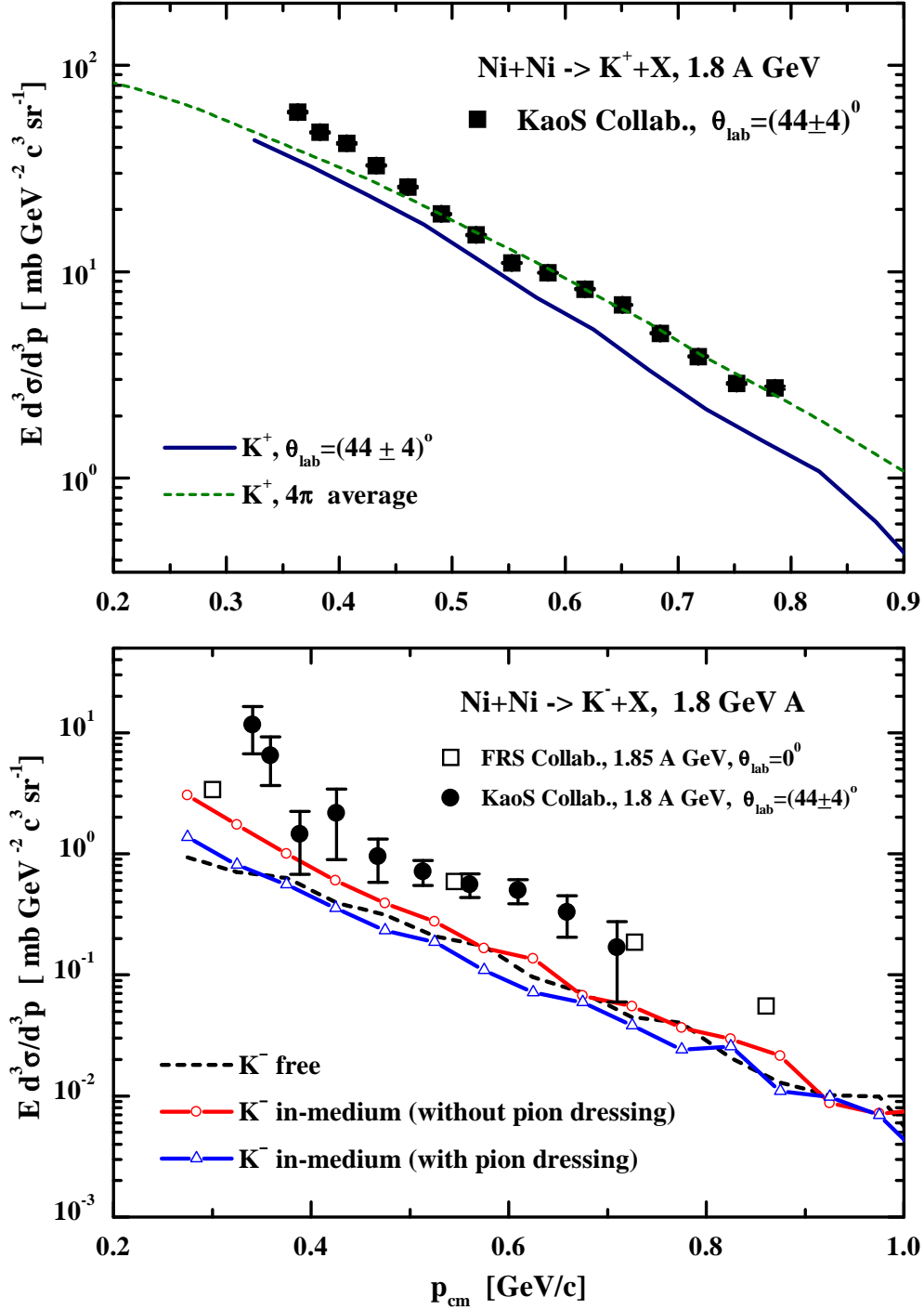


Figure 13: The differential inclusive K^+ (upper part) and K^- spectrum (lower part) for the system $Ni+Ni$ at 1.8 A·GeV and $\theta_{lab} = (44\pm 4)^0$ in comparison to the data from Refs. [82, 83]. The dashed line in the upper part reflects the result of the transport calculation after averaging the K^+ spectra over the angle Ω in the center-of-mass system, while the solid line displays the calculated spectrum for $\theta_{lab} = (44\pm 4)^0$. Lower part: The dashed line corresponds to a 'free' calculation, the solid line with open triangles to a G -matrix calculation including pion dressing whereas the solid line with open circles results from a G -matrix calculation without pion dressing.

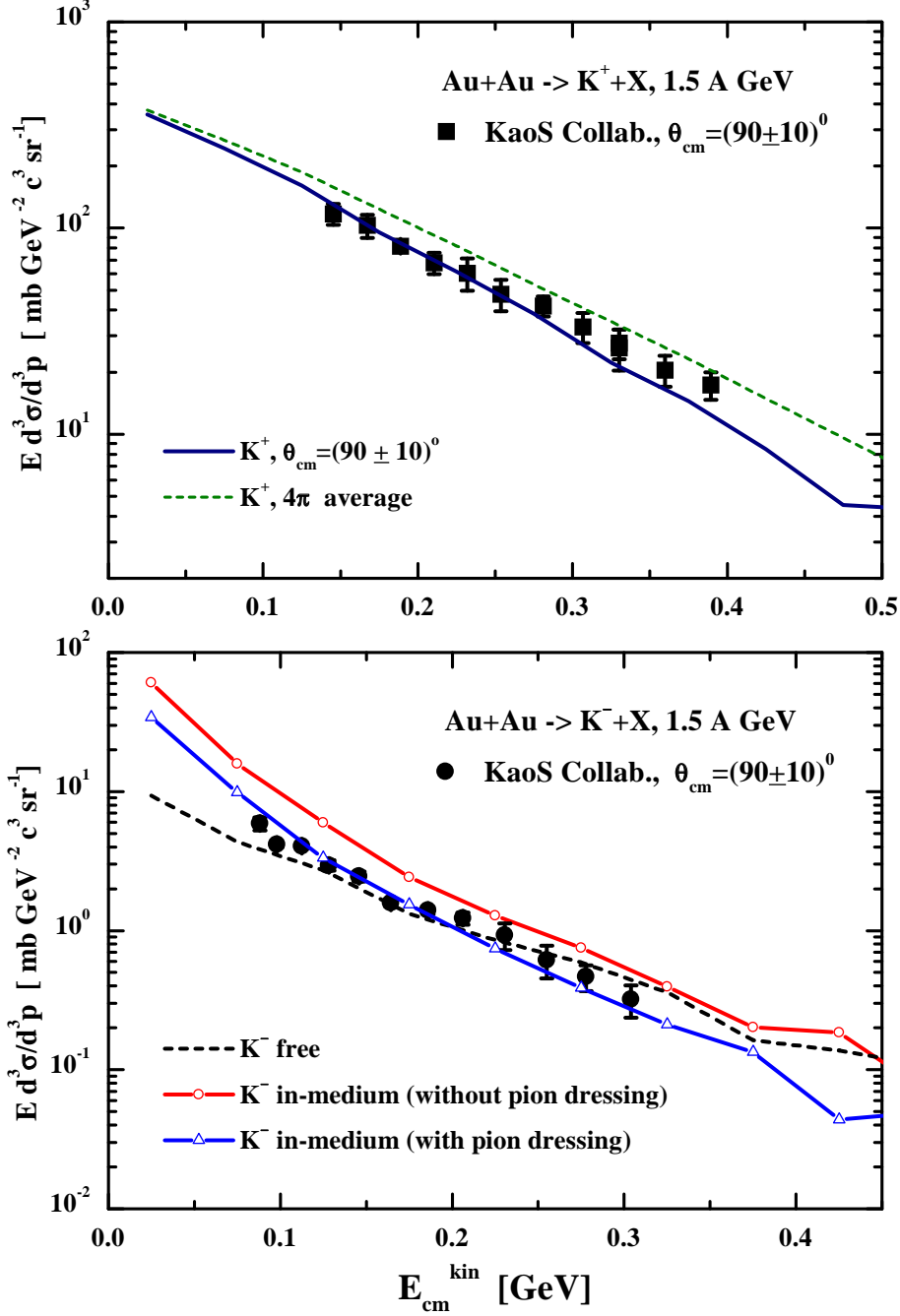


Figure 14: The differential inclusive K^+ (upper part) and K^- spectrum (lower part) for the system $Au + Au$ at 1.5 A·GeV and $\theta_{\text{cm}} = (90 \pm 10)^\circ$ in comparison to the preliminary data from Ref. [84]. The dashed line in the upper part reflects the result of the transport calculation after averaging the K^+ spectra over the angle Ω in the center-of-mass system, while the solid line displays the calculated spectrum for $\theta_{\text{cm}} = (90 \pm 10)^\circ$. Lower part: The dashed line corresponds to a 'free' calculation, the solid line with open triangles to a G -matrix calculation including pion dressing whereas the solid line with open circles results from a G -matrix calculation without pion dressing.

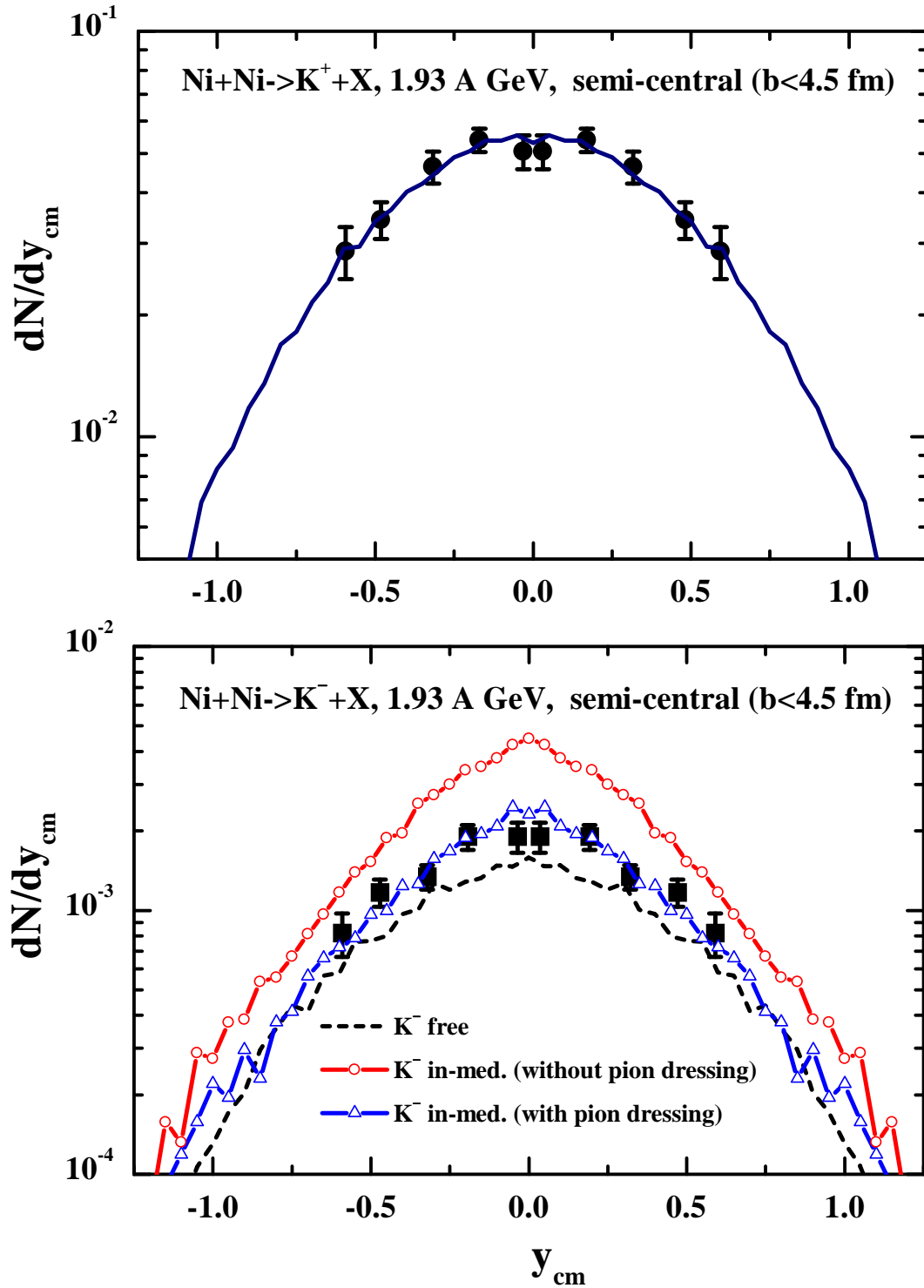


Figure 15: The rapidity spectrum of K^+ (upper part) and K^- mesons (lower part) for the system $Ni+Ni$ at 1.93 A·GeV and semicentral collisions ($b \leq 4.5$ fm) in comparison to the data from Ref. [85]. The dashed line (lower part) corresponds to a 'free' calculation, the solid line with open triangles to a G -matrix calculation including pion dressing whereas the solid line with open circles results from a G -matrix calculation without pion dressing.

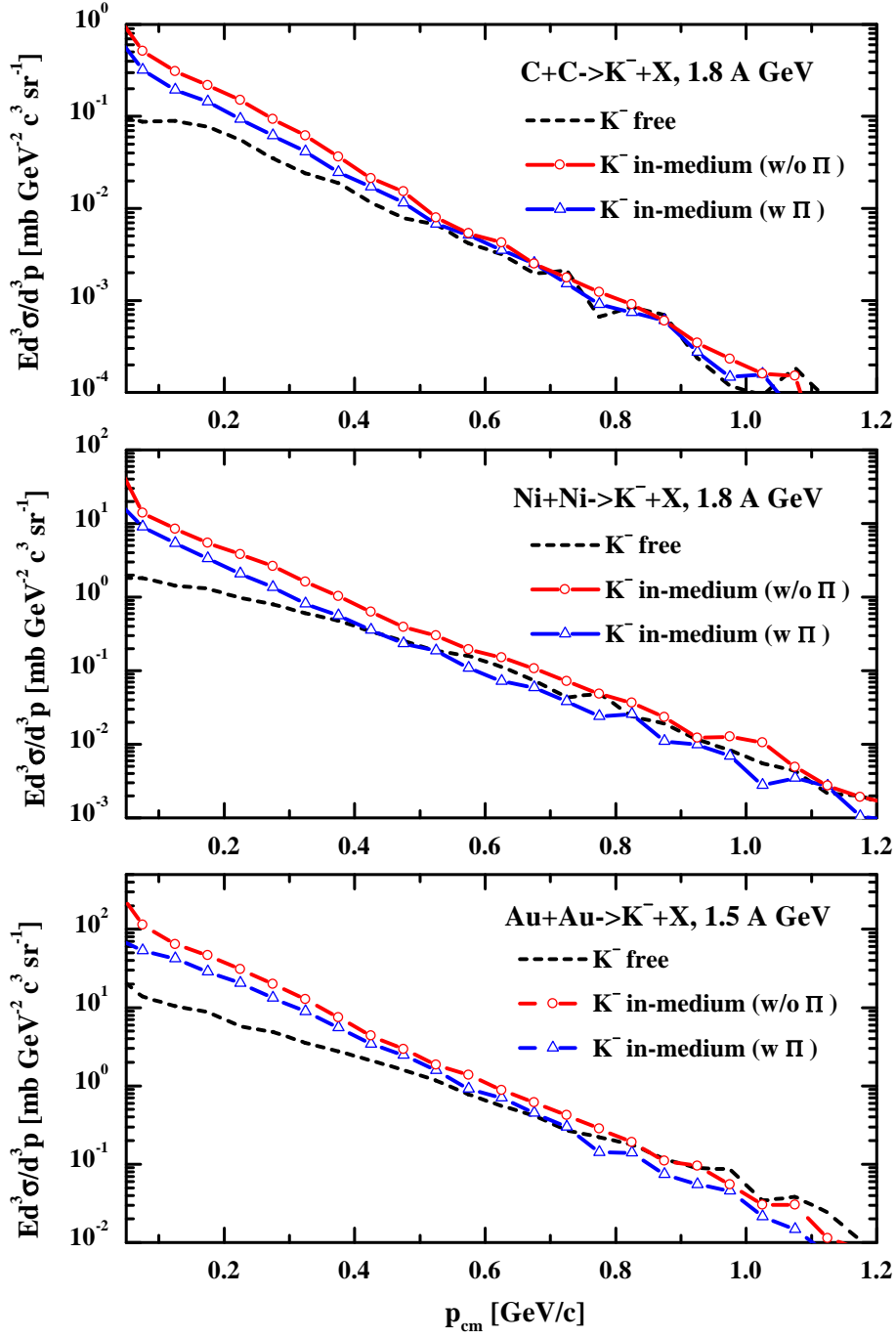


Figure 16: The inclusive momentum spectrum of K^- mesons for the systems $C + C$, $Ni + Ni$ and $Au + Au$ as a function of the antikaon momentum in the center-of-mass system p_{cm} . The dashed lines correspond to a 'free' calculation, the solid lines with open triangles to G -matrix calculations including pion dressing whereas the solid lines with open circles result from G -matrix calculations without pion dressing.

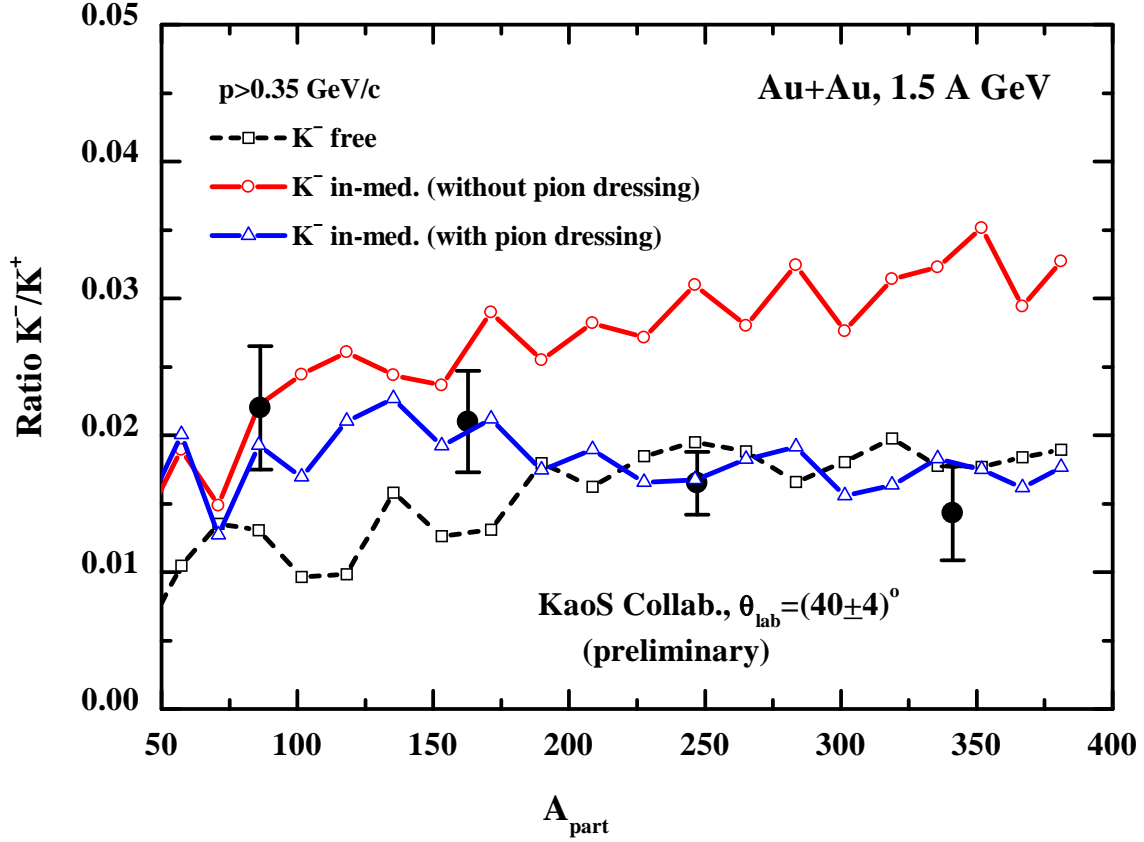


Figure 17: The K^-/K^+ ratio as a function of centrality, expressed in terms of the number of participating nucleons A_{part} , for the system $Au+Au$ at $1.5 A \cdot \text{GeV}$ and $\theta_{cm} = (90 \pm 10)^\circ$ including a cut in momentum $p_{cm} \geq 0.35$ GeV/c. The preliminary experimental data have been taken from Ref. [84]. The dashed line corresponds to a 'free' calculation, the solid line with open triangles to a G -matrix calculation including pion dressing whereas the solid line with open circles results from a G -matrix calculation without pion dressing. The fluctuations of the lines are due to the limited statistics.

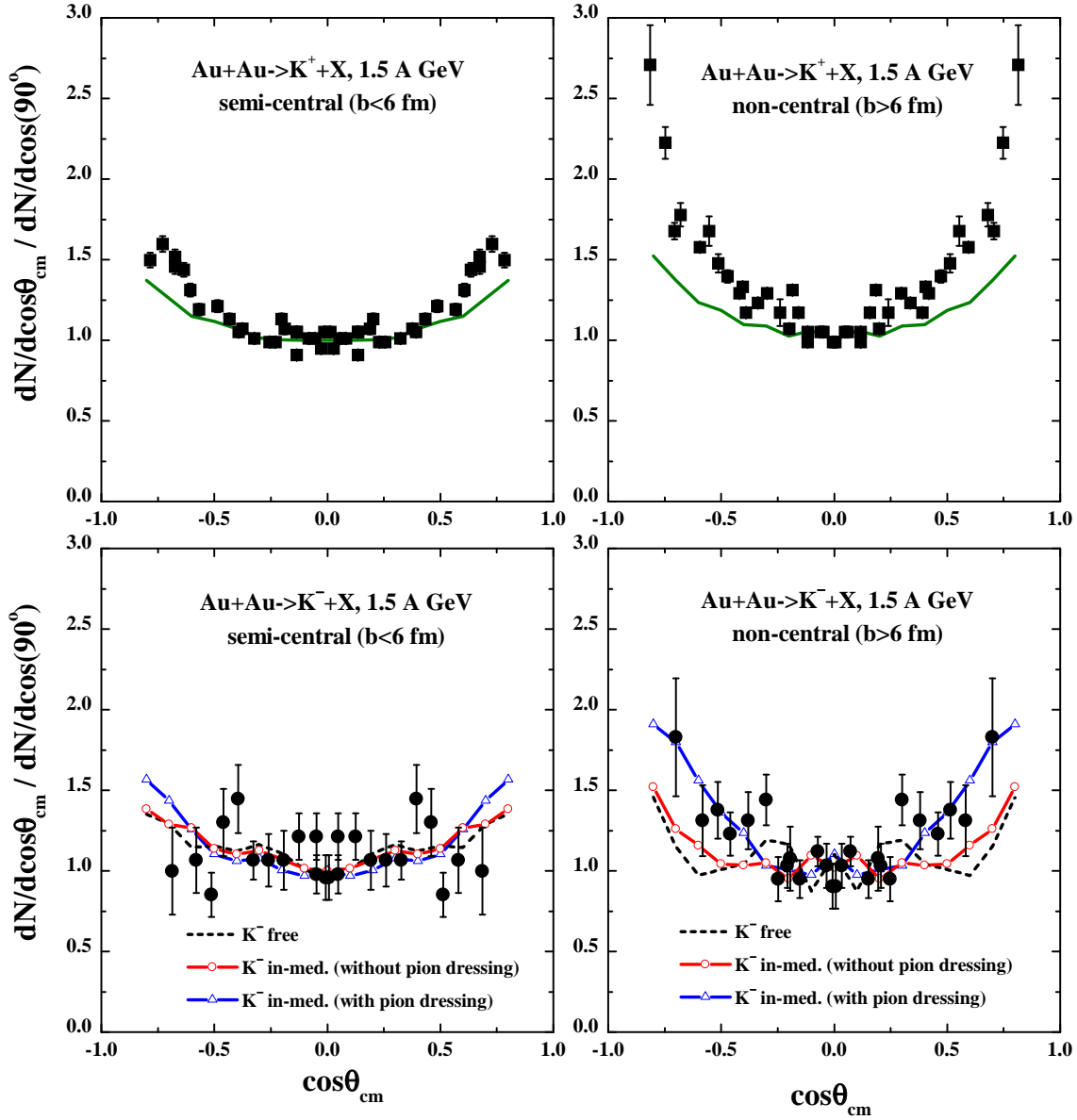


Figure 18: The K^+ (upper part) and K^- angular distribution (lower part) for semi-central (l.h.s.) and non-central (r.h.s.) $Au+Au$ collisions at 1.5 A·GeV. All angular distributions are normalized to unity for $\cos\theta_{cm} = 0$. The preliminary experimental data have been taken from Ref. [88]. The dashed line corresponds to a 'free' calculation, the solid line with open triangles to a G -matrix calculation including pion dressing whereas the solid line with open circles results from a G -matrix calculation without pion dressing. The fluctuations of the lines for the K^- angular distributions are due to the limited statistics again.